Scanning Tunneling Microscopy Studies of Metal on Metal Epitaxy

Robert Q. Hwang* and Maria C. Bartelt

Sandia National Laboratories, Livermore, California 94551

Received March 4, 1997 (Revised Manuscript Received April 16, 1997)

Contents

I. Introduction

Metal films are crucial in nearly all current technologies ranging from microelectronics and data storage to protective coatings. These applications take advantage of the wide suite of unique phenomena that films exhibit, including novel chemical, magnetic, and mechanical properties. While research in manipulation of film growth has been active for many decades, much of the recent research aimed at controlling film properties is directed specifically at identifying and characterizing key physical processes that determine the details of film structure and composition. Prior to the advent of the scanning tunneling microscope (STM),[1] most experimental studies measured average properties such as overall chemical composition and long-range periodic structure using techniques such as electron- and photon-based spectroscopies and diffraction. Dynamic aspects of morphology had been investigated using electron microscopy, but resolution limitations restrict access to the fundamental atomic processes that govern film growth. Processes such as adatom diffusion have been investigated with field ion microscopy (FIM);[2] however, only the motion of single atoms or clusters of a few atoms can generally be followed.

The effectiveness and current dominance of STM in the study of metal-on-metal systems is primarily due to two characteristics. First, STM provides real-space imaging so the influence of nonperiodic structures can be studied. This includes the role of surface steps, dislocations, and impurities. Second, STM provides a wide range of spatial resolution, from atomic level imaging to several micrometers. This is particularly important to understand the relationships between atomic processes and final film structure and morphology. Basic relationships have been validated, discarded, and discovered through fervent research in the last few years. Through such work, a clear conclusion has arisen that large observable consequences do follow from subtle changes in atomic processes.

This article reviews selected contributions that STM has made in the understanding of metal-on-metal epitaxy. This is presented not from a historical perspective but rather by highlighting key scientific issues that STM has and will continue to impact. The paper is divided into three topic areas: nucleation, structure, and composition. This is done only for organizational purposes and not to imply that they can be viewed distinctly. There exist fundamental interactions between all of these phenomena that lead to the rich behavior in metal films highlighted

Robert Hwang was born in Macao, in 1961. He received his B.S. from UCLA in physics in 1981. His graduate thesis was on surface-phase transitions and was completed in 1988 at the University of Maryland under Ellen Williams and Robert Park. He then went on to a postdoctoral appointment in the group of Gabor Somorjai at UC Berkeley where he also worked closely with Michel van Hove and Miquel Salmeron. In 1990 he received a Humboldt fellowship to work with Juergen Behm at the University of Munich where he began studying metal epitaxy. In 1991, he joined Sandia National Laboratories where he is presently a senior member of the technical staff.

Maria Bartelt was born in Malange, Angola, in 1961, and grew up in Luanda (with her identical twin). She graduated from the University of Oporto, Portugal, in 1984, with a thesis on the statistics of percolation clusters supervised by José Duarte. She received Master's (1989) and Ph.D. (1991) degrees in physics from Clarkson University, Potsdam, NY, working with Vladimir Privman on surface effects in statistical mechanics. She then held a postdoctoral appointment in James Evans' group at Iowa State University, studying epitaxial film growth until 1996. At Sandia National Labs, she is part of the Computational Materials Science program addressing interconnect reliability and its links to thin-film microstructure and dynamics.

S0009-2665(96)00070-2 CCC: $28.00

throughout the article. One of the great contributions of STM has been precisely to discover these links.

II. Nucleation and Growth

Central to many studies of film nucleation, growth, and coarsening has been to relate features of film morphology to the underlying attachment/detachment and diffusion mechanisms. From an experimental standpoint, this typically involves systematic characterization of films obtained under a variety of controlled deposition conditions. Theoretical progress has been somewhat slower, largely due to the intricate nature of nonequilibrium effects. For metals, the coupling between experiment based on STM and theory has been uniquely successful. In this section, we review very basic concepts that aid in formalizing nucleation issues at surfaces and illustrate their development through some of the most interesting systems.

The morphology of a metal film has traditionally been catalogued by one of three idealized types of growth modes: continuous 2D layer-by-layer or Frank−van der Merwe growth, 2D layer-by-layer followed by 3D island formation or Stranski−Krastanov growth, and finally 3D island formation or Vollmer−Weber growth.[3] These different structures reflect the thermodynamic properties of the film, substrate and interface in the following way. Thermodynamic equilibrium requires that the system be in its lowest free energy configuration. For a film, the system energy can be considered a sum of three parts: the surface free energy of the film (γ_f), the surface free energy of the substrate (γ_s), and the free energy of the film/substrate interface (γ_i). If the sum $\gamma_f + \gamma_i$ is greater than γ_s, the overlayer will form 3D islands so as to minimize the total energy by exposing more of the substrate. If on the other hand $\gamma_f + \gamma_i$ is significantly smaller than γ_s, the substrate will be completely covered by the overlayer and layer-by-layer growth occurs. In general, true layer-by-layer growth is only expected for homoepitaxy ($\gamma_s = \gamma_f + \gamma_i$). In heteroepitaxy, layer-by-layer growth usually converts to 3D island formation at some film thickness since overlayer and interface free energies change with the film thickness, i.e., Stranski−Krastanov growth is the most commonly found growth mode.

These equilibrium concepts have to be tempered by the fact that film growth during deposition is inherently a nonequilibrium process, i.e., the final film structure and morphology depend on the extent to which certain atomic processes are effectively "frozen" during deposition. The resulting film morphology is always more complex owing to the competition between thermodynamics and kinetics. These complexities can be appreciated within a highly conceptual yet very useful picture of how a film grows. Consider a crystalline substrate as shown in Figure 1a. The surface consists of atomically flat terraces separated by steps also of atomic dimensions. During deposition, atoms land on the surface at a controlled rate. Once on the surface, they migrate between adsorption sites at some system-dependent diffusion rate, D. These mobile "adatoms"

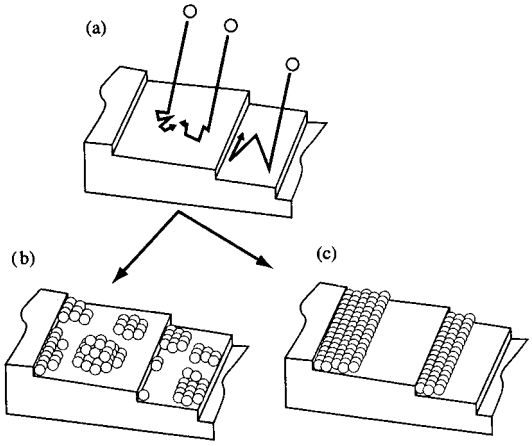

Figure 1. Atom deposition and aggregation during MBE: (a) Substrate surface consists of atomically flat terraces separated by steps. Deposited atoms land and diffuse on terraces. (b) Island nucleation and growth results from adatom−adatom and adatom−island encounters. (c) Aggregation at steps may dominate at lower flux. (Reprinted from ref 79. Copyright 1995 IBM.)

form a lattice gas on the surface, and incorporate into the "solid" in two primary ways: adatoms can aggregate and form islands on terraces upon meeting with other adatoms (Figure 1b) or they can attach to step edges (Figure 1c). (Of course under realistic experimental conditions, a myriad of other processes can occur: atoms can also diffuse along island or step edges, detach from islands or steps thereby returning to the adatom gas, etc.) Even within this simple picture, one can see how important the competition between these processes is to the final film morphology. When atoms predominantly attach to step edges, the film grows by step flow, repeating the substrate morphology at the completion of each monolayer (Figure 1c). This scenario is anticipated whenever the characteristic adatom diffusion length on terraces, which is controlled by substrate temperature and deposition flux, is comparable to the width of the terraces. However, on "wide" terraces, 2D island formation far from steps is generally observed. With continued deposition, these islands grow and coalesce, and second layer islands typically nucleate before the first layer is complete. This leads to (kinetic) roughening of the multilayer film, typically in the form of mounds or pyramids, whose structure can be very sensitive to that of the submonolayer "template". Here too, STM has proven extremely valuable at providing quantitative information on island distributions within each layer, their dependence on external parameters, temperature and deposition flux, and on the strong dependence on any restrictions to interlayer transport.

An important application of STM has been to actually observe islands, their shapes, areal coverage, size, and spatial distributions on the atomic length scale. These data are vital to test the above concepts and extract information about atomic processes. To this end, the key method was performing measurements at different controlled values of the deposition parameters, specifically temperature and flux. Stroscio and Pierce used this approach to investigate the homoepitaxial growth of Fe on Fe(001).[4,5] Figure 2a−f displays a series of STM images of 0.07 monolayer

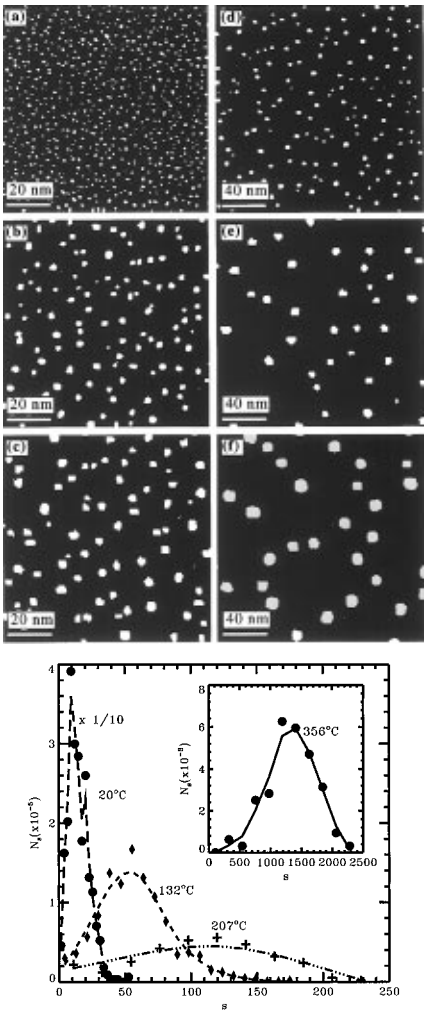

Figure 2. (top) STM images (100 × 100 nm^2) of single layer Fe islands (white) on the Fe(100) surface (black). Sample temperatures for the different panels were (a) 20 °C, (b) 108 °C, (c) 163 °C, (d) 256 °C, (e) 301 °C, and (f) 356 °C. (bottom) Fe island size distributions corresponding to the data from a; s is in atoms; N_s is per site. (Reprinted from ref 5. Copyright 1991 American Institute of Physics.)

(ML) Fe films grown at a rate of 0.012 ML/s, at different substrate temperatures. From this type of data, the island size distributions as a function of temperature are shown in Figure 2. The authors demonstrated an Arrhenius dependence of the average island size (or the average island density) on temperature, suggesting a connection between island nucleation and thermally activated processes on the surface. One such connection is easy to envision: the higher the temperature, the higher the probability that a deposited atom reaches a step edge or an existing island before the next atom is deposited. This results in a lower island density.

Prompted by the availability of this type of data, theoretical approaches have been developed to assist in their interpretation. These fall into two classes: Monte Carlo simulations of suitable lattice−gas models[6−12] and increasingly more sophisticated mean-field rate-equation treatments.[13,14] With few exceptions,[10−12] analyses of island formation during film deposition typically assume the existence of a well-defined integer, i, above which islands are effectively stable against dissociation. Rate-equation[13,15] and simulation[6−9] studies then predict that the average island density, N, is given by

$$N \approx \eta(\theta)(F/\nu)^{\chi} \exp\left[\frac{\chi[E_d + (E_i/i)]}{k_B T}\right] \qquad (1)$$

Here $\chi = i/(i+1)$, E_d is the energy barrier for (isotropic) diffusion of isolated adatoms and ν is the associated attempt frequency so that the diffusion rate is $D = \nu a^2 \exp(-E_d/k_B T)$, a being the lattice constant. E_i is the binding energy of the critical island of size i, and $\eta(\theta)$ is weakly dependent of the fractional film coverage, θ. T is the temperature and F is the deposition flux rate (which sets the time scale). Thus in principle, i can be estimated from the dependence of N on F, at fixed T and θ. At "low" temperatures where island formation can be considered irreversible, ($i = 1$, $\chi = 1/3$, $E_1 = 0$), the Arrhenius slope of N then yields E_d. Extraction of E_i from the decrease of N with further increasing T (or decreasing F) is possible provided the system is studied in regimes of well defined $i > 1$. In practice, this is not guaranteed, and broad transition regions separate brief regimes of different i. In this case, simulations must be used to analyze observed behavior.[11,16,17]

Recent criticism has been raised of the estimates of E_i from using (1) to model the Arrhenius slope of STM data at high temperature.[18] Feibelman suggested that the value $E_3 = 1.1 \pm 1.0$ eV extracted for Fe/Fe(100)[5,9,16] is too large due to neglect of different diffusion mechanisms that may take place in different temperature ranges. Presumably, this switch in diffusion mechanisms with increasing temperature would not be unique to the Fe/Fe(100) system. Similar criticism applies to current estimates for other metals, to estimates from effective medium-type and first principles calculations, or from analyses of equilibrium island shapes using nearest-neighbor pair interaction models.[17,19,20] The criticism relies on comparison with a FIM measurement of the bond energy of W addimers on W(110), and the expectation that the adatom−adatom bond strength for simple metals should scale like their bulk cohesive energies.[18] While competition between various diffusion mechanisms on metal surfaces at high temperatures may be important, resolution will more likely involve reassessment of the validity of short-range "two-body" potentials to describe island stability during metal-on-metal epitaxy.[19]

More detailed predictions for the adlayer morphology are available from simulation studies.[7,11] In particular, they anticipate the existence of nontrivial scaling forms for the island size and separation distributions. These forms depend strongly on i, and some details of island shape and mobility, features that can be exploited in modeling.[21]

One of the first applications of these concepts to an STM study was by Stroscio and Pierce for the Fe/Fe(100) data shown in Figure 2. Assuming $i = 1$ below 250 °C, the Arrhenius slope of N gives $E_d = 0.45 \pm 0.04$ eV from (1). This interpretation has received strong support from simulations,[7,17] which match not only the actual values of N, but also key features of the observed island size and separation distributions using the extracted E_d above, $\nu \approx 10^{11}/s^{-1}$ and the experimental values of θ, F, and

T. Note that this method does not identify the dominant diffusion mechanism, only its activation barrier and preexponential factor.

Other STM studies of island formation have appeared, addressing similar behavior in both homoepitaxial (Ag(100),[19] Ag(111),[22] Ni(100),[23] Pt(100),[24] Pt-(111),[25] and Rh(111)[26]) and heteroepitaxial (Ag/Pt(111),[27] Cu/Ni(100)[28]) systems. In some instances, values of E_d derived from these STM studies have already been confirmed by FIM.[2]

On many surfaces, other processes such as atomic exchange between adatoms and substrate atoms can have a strong influence on nucleation. This is found in the case of Ni growth on Ag(111) studied by Meyer and Behm.[29] Upon measuring the nucleation density of islands as a function of temperature, they found that contrary to the expected result of conventional nucleation theory, the island density increased with increasing temperature. The cause of this apparently contradictory result is that at higher temperatures place exchange between deposited Ni atoms and substrate Ag atoms can take place. These incorporated Ni atoms act as nucleation sites for islands, thus increasing the island density. This conclusion was corroborated by simulations which allowed the authors to estimate the energy barrier for place exchange to be between 0.6 and 0.9 eV.

A natural extension of the submonolayer STM studies is the examination of the subsequent multilayer kinetic roughening of these metal films. Here, important issues relate to assessment of interlayer transport, specifically of additional barriers to downward diffusion at step or island edges, and of the role of surface geometry. Analysis of the selected film structure at various *T* (or *F*), in comparison with simulation predictions, can provide such information. The presence of step-edge barriers is expected to induce the formation of mound or pyramid instabilities,[30] due to reflection of diffusing adatoms at descending steps and thus biased incorporation at ascending steps. On the other hand, the metal adsorption-site geometry and related aspects of the deposition dynamics (such as downward deflection or "funneling" of atoms deposited at edges or small microfacets[31,32]) place severe constraints on film roughness, and are believed to stabilize the mound slopes in these systems.[33,34]

At room temperature, Stroscio et al. indeed found that the Fe/Fe(100) films roughen into an array of mounds of fixed average slope, which coarsen as the films thicken.[35] (See the STM image in Figure 3.) While quantitative understanding of some aspects of this coarsening process is still emerging, many of the observed features of the Fe/Fe(100) films in the range of 1−100 ML have been reproduced essentially exactly by simulations extending the submonolayer description of island nucleation and growth to the multilayer regime, and incorporating a step-edge barrier and a realistic treatment of geometry effects.[33,34,36] These simulations predict an effective (additional) step-edge barrier of about 10% of E_d for Fe/Fe(100) (assuming a common $\nu \approx 10^{11}/s^{-1}$). Other metal (100) homoepitaxial systems show behavior consistent with similarly "low" effective step-edge barriers[19] (with the possible exception of Cu[17]). This is unlike unreconstructed metal (111) systems where

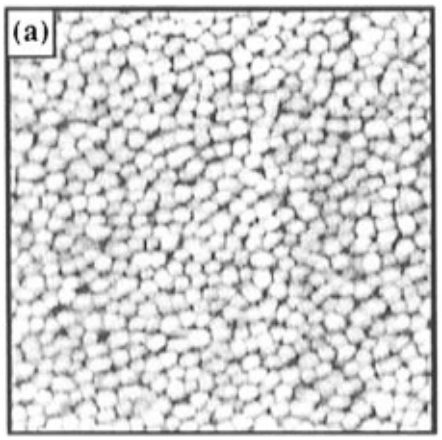

Figure 3. Mound formation in the growth of Fe on Fe-(100). Panel is (100 × 100 nm^2) STM image of 10 ML of Fe on Fe(100) deposited at 20 °C. Total vertical range is 0.9 nm. (Reprinted from ref 35. Copyright 1995 American Institute of Physics.)

typical observation of "very rough growth" for some range of *T* suggests significantly higher step-edge barriers (but also more complex dependence of these on step-edge structure).[37,38]

Compared to rate-equation treatments of submonolayer island formation, rate equations capable of predicting island distributions during multilayer growth are largely underdeveloped. Early attempts date back to refs 39−43. Much of the difficulty arises when trying to accurately describe deposition events on real adsorption site geometries, island coalescence and percolation, possible rapid island shape restructuring upon coalescence (and its strong influence on the onset of next layer population), the kinetics of vacancy filling near layer completion, etc.

Recent efforts focused on obtaining layer coverage distributions just at the onset of second-layer nucleation.[44,45] The basic result relates system parameters (including the step-edge barrier) to the smallest first-layer coverage, θ_c (or, alternatively, average island radius) above which second-layer nucleation occurs. θ_c can be determined directly with an STM. Estimates of the step-edge barrier via this approach are overly sensitive to the estimate of θ_c, but for all cases studied, they are qualitatively consistent with results from benchmark simulations.[45]

A complementary mean-field analysis, not yet tested with simulations, has proposed a relatively simple formula to account for the dependence on island size of the fraction, $1 - \exp(-s/\tilde{s})^{\sigma}$, of islands of size *s* on top of which second-layer islands (of any size) have nucleated.[46] Here, $\tilde{s}$ and σ contain information on system parameters. This result is intrinsically limited to the precoalescence regime.

Bromann et al.[47] recently designed specific STM experiments to directly apply this formula. They first obtained a sharp island size distribution in the first-layer of each sample via controlled annealing, and then produced second-layer islands by depositing further material in amounts too small to significantly change the starting size distribution. Although "tailoring" the island sizes is not required by the theory, it greatly simplified the STM analysis. Estimates were obtained for the effective additional step-edge barriers in Ag/Ag(111) and Ag/1ML Ag/Pt-

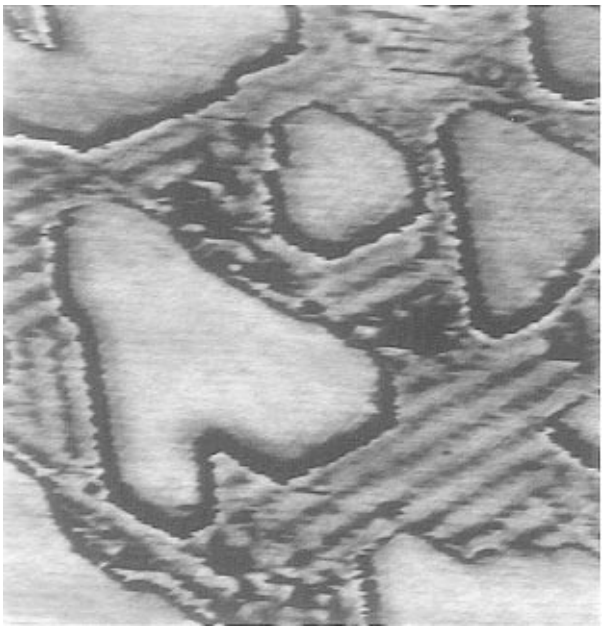

Figure 4. A (100 × 100 Å^2) STM image of Au islands deposited on a p(2×2) O-precovered Ru(0001) surface. The presence of Au compresses the O structure to a p(2×1) phase as can be observed by the O rows between the Au islands. (Data taken from ref 48.)

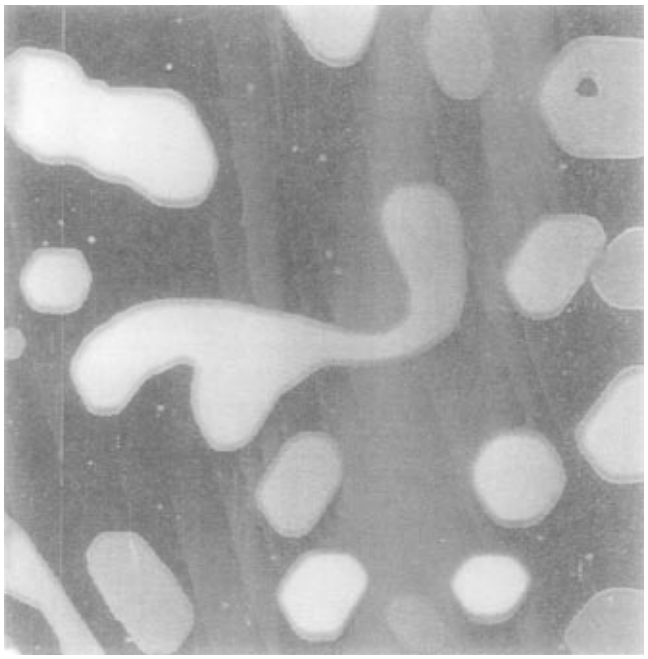

Figure 5. STM topograph of an approximately 5 ML Au film deposited on a p(2×1) O precovered Ru(0001) substrate following annealing to 800 K (1600×1600 Å^2). (Reprinted from ref 49. Copyright 1992 American Vacuum Society.)

(111). The former (~129 meV[47]) is even larger than the terrace diffusion barrier (~97 meV[27]), consistent with the common observation of very rough growth in this system.[37] No information can be extracted with this method about (expected) nonuniformities in the step-edge barrier around the island perimeter.

Impurities are also known to greatly affect film growth both thermodynamically and by altering atomic kinetics. To investigate this phenomenon in a controlled manner, several groups have studied island nucleation on surfaces precovered with precise amounts of another species. For example, Schröder et al. compared the nucleation and growth of Au on Ru(0001) with that on an oxygen-precovered substrate.[48] Au nucleation densities were found to increase by over 10^4 in the presence of oxygen. Atomically resolved images reveal the mechanism that caused the effective reduction in the Au diffusion rate in the presence of oxygen. In order to migrate, Au atoms must displace oxygen atoms, leading to a lower Au diffusion rate and compression of the oxygen layer on the Ru surface. No oxygen was found on the Au islands. This is shown in Figure 4 in which an initial p(2×2) coverage of oxygen is compressed to a p(2×1) structure as indicated by the stripes of oxygen between the Au islands. At higher Au coverages, the presence of oxygen has a pronounced effect on the thermodynamics. It is known that on the clean Ru(0001) surface, Au grows in a Stranski−Krastanov mode, i.e. layer-by-layer growth followed by 3D clusters. On the oxygen-precovered surface however, the growth mode changes to pure 3D mode, or Vollmer−Weber growth. Upon annealing of a 5 ML film, Au islands configure into multilayer structures, exposing large areas of the oxygen-covered substrate (Figure 5).[49] The basic driving mechanism for this is the lowering of the surface free energy of Ru(0001) due to adsorbed oxygen. Thus the overall minimum energy configuration of this

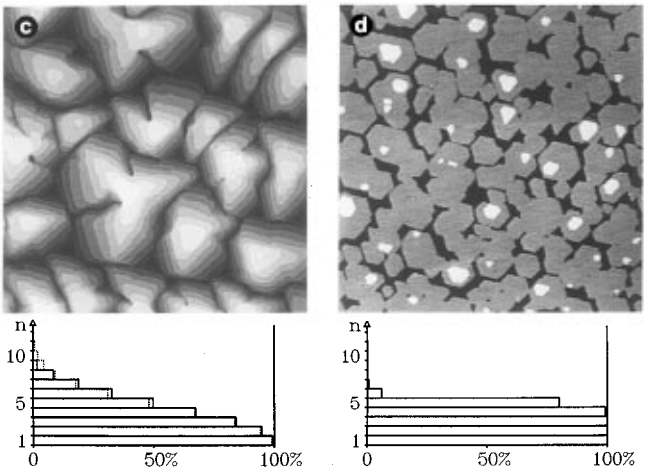

Figure 6. Topographs (2200 × 2200 Å^2) taken after deposition of approximately 5 ML of Pt at 400 K on (a, left) clean Pt(111) surface, (b, right) oxygen-precovered surface. The percentage completion of the layers versus layer number, *n*, is plotted in the hisotgrams below each image. (Reprinted from ref 50. Copyright 1994 American Institute of Physics.)

system is one that leaves the oxygen-covered surface as exposed as possible.

In other systems, oxygen can have the reverse effect and act as a surfactant, i.e. enhance layer-by-layer growth. Esch et al. investigated the effects of oxygen in the homoepitaxy of Pt on unreconstructed Pt(111).[50] On the clean substrate, deposition of 5 ML of Pt at 400 K results in the film shown in Figure 6a. Mounds are formed with multiple layers exposed. However, with a small precoverage of oxygen, the identical deposition conditions produce the film shown in Figure 6b. The surface is dramatically smoother, with only three layers exposed. This is quantified in the histograms of Figure 6 which show the fractional population of each layer for the two films. As in the case of Au/O/Ru(0001), the Pt island density

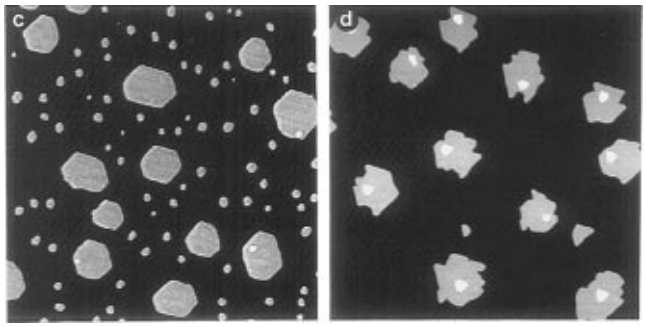

Figure 7. Topographs (2200 × 2200 Å^2) taken after an additional growth step on islands of nearly the same size: (a, left) oxygen covered, and (b, right) clean surface. (Reprinted from ref 50. Copyright 1994 American Institute of Physics.)

increases substantially in the presence of oxygen. However, here the growth of Pt islands does not lead to compression of the oxygen phase. Instead, oxygen atoms migrate to the surface (no indication of bulk incorporated oxygen was found). One possible explanation for this surfactant behavior is the purely geometric effect that the smaller size of Pt islands in the presence of oxygen inhibits next layer nucleation. However, this is not the dominant effect. When growing islands of similar size on both the clean and oxygen precovered surface, nucleation of next layer islands was much more likely on the clean surface, despite the fact that the oxygen on the islands reduces the mobility of the Pt adatoms. This is shown in Figure 7. It was therefore concluded that the oxygen reduces the effective barrier for Pt atoms to descend at the step edge. Thus interlayer transport is enhanced, aiding layer-by-layer growth.

Surfactant behavior was also observed for the homoepitaxial growth of Ag on Ag(111) with the addition of Sb.[51,52] The STM investigation performed by Vrijmoeth et al.[53] showed that this originates from a combination of two effects. First, the Sb surface segregates and lowers the mobility of Ag (by increasing the diffusion barrier) both on terraces and on top of growing Ag islands (cf. ref 54). This has the effect of reducing the additional edge barrier (the barrier to descend a step minus the surface diffusion barrier) for an Ag atom to descend a step. Second, the Sb reduces the Ag mobility around the edge of an island, thus leading to dendritic shapes. These shapes enhance layer-by-layer growth by the fact that their ratio of surface area to edge length is greatly reduced, thus decreasing the probability that further nucleation occurs on top of them. This latter effect was first observed for the homoepitaxial growth of Pt on Pt(111) where near layer-by-layer growth was induced by lowering the substrate temperature.[55,56]

Information on atomic kinetics can also be obtained by examining the shapes of nucleated islands. Very different island shapes can occur in metal epitaxy, as is demonstrated in the comparison of the two growth systems shown in Figures 8 and 2. Submonolayer deposits of Au on Ru(0001)[57] and Fe on Fe(001)[4,5] are displayed and each of the islands is of a single atomic height. For both systems, the first layer is known to wet the surface. However, the shapes of the islands that form are quite different. The Fe islands exhibit a compact, nearly square shape reflecting the 4-fold symmetry of the (100) surface, with island edges oriented along [110] directions. In contrast, the Au islands are ramified, with no apparent influence of the triangular symmetry of the substrate. This difference reflects differences in the ability of the atoms to diffuse along the edges of islands and around corners, between consecutive adatom attachments to the island. In the case of Fe, atoms arriving at the islands have enough mobility along the edge to find energetically favorable kink sites, and thus maintain near-equilibrium compact island shapes as the islands grow. On the other hand, it is clear that Au atoms deposited at room temperature on Ru(0001) do not have enough edge mobility, so the island shape cannot relax. This is supported by the fact that upon annealing, these islands achieve more compact shapes (Figure 9) without substantial transfer of atoms between is-

Figure 8. STM topograph of a 0.37 ML Au film on Ru(0001) deposited at room temperature (9300 × 10 300 Å^2). (Reprinted from ref 49. Copyright 1992 American Vacuum Society.)

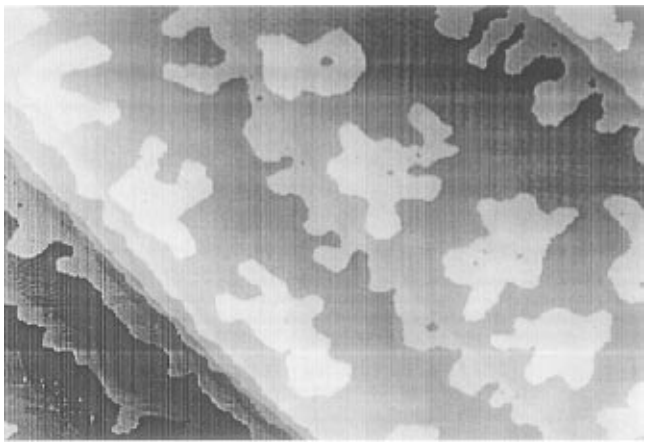

Figure 9. Image of the identical film shown in Figure 8 after annealing to 650 K (8300 × 5400 Å^2). (Reprinted from ref 57. Copyright 1991 American Institute of Physics.)

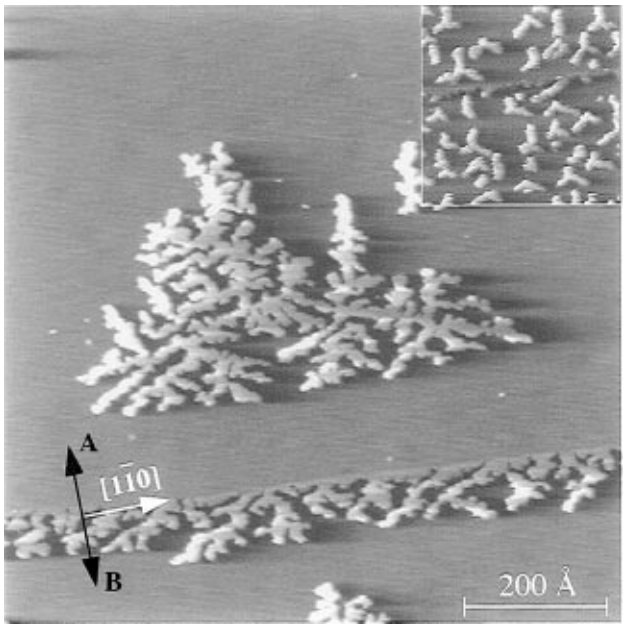

Figure 10. STM image showing dendritic Ag aggregates grown on Pt(111). (Reprinted from ref 59. Copyright 1996 North-Holland Elsevier.)

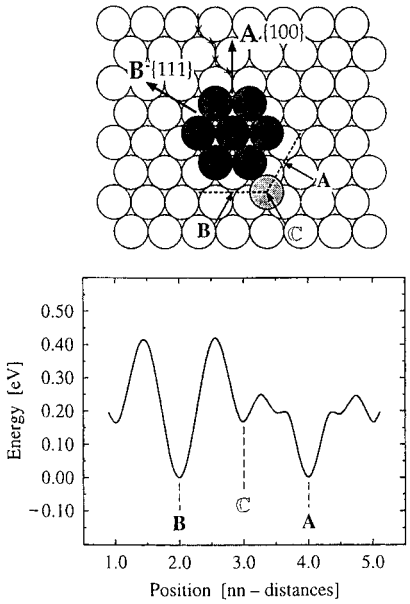

Figure 11. Difference in total energy of a Ag adatom diffusing around a Ag heptamer on Pt(111) as calculated within the effective medium theory. A and B directions are indicated in the ball model. The diffusion path with the lowest barrier is the one from the corner (C) to the hcp site close to it, at an A step. (Reprinted from ref 59. Copyright 1996 North-Holland Elsevier.)

lands (Ostwald ripening). The ramified islands are a realization of the diffusion limited aggregation (DLA) model in 2D. The premise of DLA is that once free atoms (or clusters of atoms) reach an island edge, they are trapped and can neither migrate along the edge nor detach. This process produces islands of fractal shapes with universal fractal dimension of about 1.7.[57] Standard fractal analysis of the Au island shapes has confirmed this fractal dimension, corroborating the above atomistic picture of growth on Ru(0001).

Because edge diffusion is thermally activated the development of nonequilibrium island shape instabilities should be generally important in epitaxy at "low enough" temperatures. However, the situation can be much more complicated than for Au/Ru(0001). For instance on Pt(111), Pt and Ag ramified islands grow but with highly anisotropic envelopes. This issue has been investigated in detail by Hohage et al.[58] and Brune et al.,[59] using low-temperature STM. Shapes of Ag and Pt islands on Pt(111) reflect the 3-fold symmetry of the substrate as shown in Figure 10, with branches growing preferentially in the [1$\bar{1}$2] directions. To understand how the anisotropy develops, consider Figure 11 which shows a schematic of a hexagonal island on an fcc(111) surface. Two types of step edges are present and labeled A and B. They differ in that they form small facets of different orientation, (111) and (100) for A and B, respectively. This structural difference leads to differing edge diffusion barriers along the two step types. The observed branching in the [1$\bar{1}$2] directions implies that atoms are preferentially trapped on A steps. Using effective medium theory (EMT), Brune et al.[53] calculated $E_A = 187$ meV and $E_B = 389$ meV for the edge diffusion barrier along the A and B steps respectively, for Ag/Pt(111). In addition, they found different diffusion barriers from the corner site to either the A or B step as illustrated in Figure 11. Note that the atom in position C can diffuse to site A through the intermediate high coordination hcp site. No such site exists between C and B, so the barrier for this latter process is expected to be larger. Indeed, EMT calculations find that $E_{C-A} = 80$ meV while $E_{C-B} = 248$ meV.[59] The value of E_{C-A} is in fact very close to the EMT value for the energy barrier of a freely diffusing Ag atom on Pt(111). This lower barrier preferentially allows more corner atoms to diffuse to A steps, thus promoting branching in the [1$\bar{1}$2] directions.

III. Structure

The structure of metal films is critical to nearly all of their physical properties. Although homoepitaxial films can reconstruct in response to surface stress, it is in heteroepitaxy that the opportunities open to derive film properties from lattice and chemical mismatch. The basic concept behind the near-equilibrium structure of the films in the simplest case is the accommodation of strain due to the lattice mismatch between the film material and substrate. The final film structure reflects the competition between the internal interactions of the film striving to maintain its bulk lattice constant and the forces imposed by the substrate working to continue its own bulk order. These principles have been nicely reviewed by van der Merwe.[60] The general framework for these ideas can be described qualitatively in the following scenario. As the initial layers of the film are deposited, the influence of the substrate is often large enough that the film adopts the lattice constant of the substrate at the cost of strain energy within its layers. As the thickness of the film grows, the strain energy also grows until a critical film thickness is reached at which it becomes energetically favorable to relieve strain by forming dislocations. In cases of severe lattice mismatch, this critical thickness is small and submonolayer islands can contain disloca-

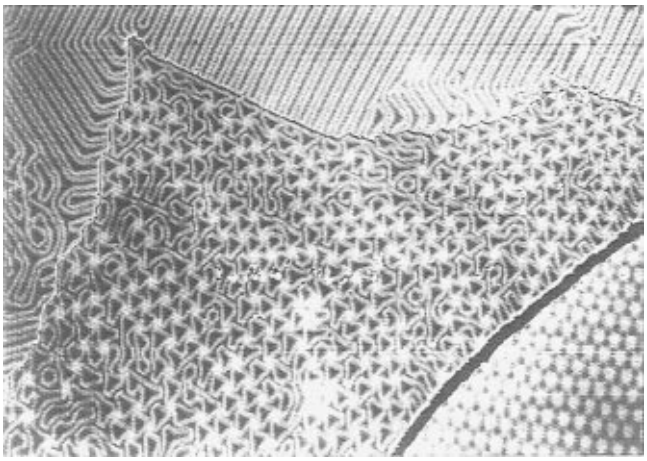

Figure 12. STM image (1930 × 1150 Å^2) of a nominally 3 ML thick Cu film on Ru(0001). Three layers are shown: second layer (upper left), third layer (central region) and fourth layer (lower right). (Reprinted from ref 61. Copyright 1995 American Institute of Physics.)

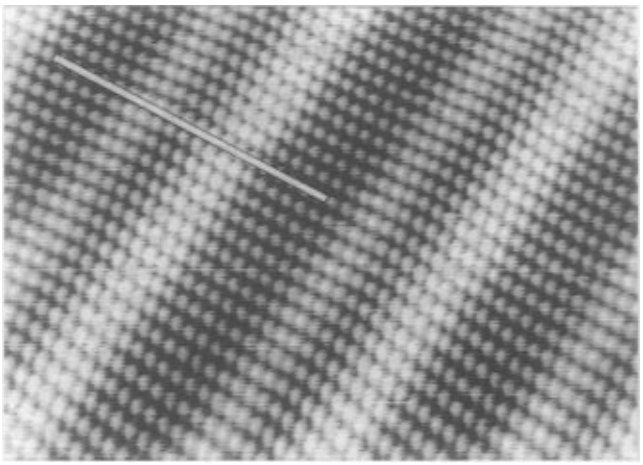

Figure 13. High-resolution STM image (95 × 65 Å^2) of the second layer striped phase of Cu on Ru(0001). (Reprinted from ref 61. Copyright 1995 American Institute of Physics.)

tions. STM has allowed both the long-range periodic structure and the atomic arrangement within and near dislocations at surfaces to be investigated.

Most of the work to date concentrates on the closed-pack surfaces of fcc and hcp materials. A prototype example is the growth of Cu on Ru(0001) where the Cu lattice constant is 5.5% smaller than that of the Ru substrate. As a function of layer, the structure of the surface takes a range of forms.[61,62] (See also ref 63 for analogous behavior in Ag/Ru(0001), and ref 27 for Ag/Pt(111).) At one monolayer, the Cu assumes a pseudomorphic structure, i.e., it adopts the lattice spacing of the Ru(0001) substrate. Subsequent layers however exhibit more complex structures as shown in Figure 12. In the second layer (upper left of Figure 12), linear stripes running in the [$\bar{2}$11] directions are found. In the third layer (central portion of Figure 12), the stripes are replaced by a trigonal network of lines. The fourth layer exhibits yet a different structure, that of a moiré pattern formed by the superposition of two triangular lattices (lower right portion of Figure 12). These series of patterns result from the increasing amount of strain relief within each subsequent layer.

Although these patterns are different and even vary in global symmetry, they are made up of a fundamental geometric structure known as a stacking fault.[64] They occur because on these close-packed surfaces two types of high coordination sites, fcc and hcp, are available for adsorption, with typically little difference in binding energy. For perfect continuation of the substrate only one type of site is occupied: fcc for an fcc substrate and hcp for an hcp substrate. However, strain is known to be relieved by the formation of domains in which the other type of site is occupied. These domains are thus referred to as stacking faults, and their formation is a fundamental response to strain. This is because of the low cost in energy to form them and the fact that strain is relieved by the atoms situated between adjoining domains of fcc and hcp stacking which must occupy intermediate nonepitaxial positions between the two binding sites. This leads to a different local atomic density in narrow transition regions, and both tensile and compressive strain can be accommodated by either a higher or lower density of atoms in these regions. These transition regions are well-known structures in materials science. They are characterized by the vector (known as the Burgers vector) defining the shift in the atoms from one type of binding site to the other as one crosses the fault. Because the vector linking hcp and fcc sites is not a full lattice vector, these faults are in fact partial dislocations.[65] The bright lines in the structures of Figure 12 are buckled regions of the film due to partial dislocations, as is clear in an atomic resolution image of the second layer structure shown in Figure 13. Tracking the atomic rows across the stripes reveals a lateral shift at the stripe of the exact amount expected for the displacement between hcp and fcc stacking regions. At the partial dislocations, the atoms reside in intermediate sites between the two high symmetry hollow sites so that they appear raised relative to the latter. Note that the widths and depths of the hcp and fcc regions (darker regions between the stripes of Figure 13) are not equal. Because of the geometry and energy differences between the two binding sites, these two regions are imaged at different depths and have unequal widths. The amount of strain relief in each subsequent layer is determined by the pattern and density of the dislocations. Because the pattern is linear in the second layer, strain is only relieved in the direction perpendicular to the stripes. In the third layer, the trigonal pattern leads to a more uniform strain relief. Finally, the moiré pattern of the fourth layer indicates nearly isotropic strain relief.

These concepts can be demonstrated in a simple mathematical model first introduced by Frenkel−Kontorowa and analyzed in detailed by Frank and van der Merwe.[66] The model represents the overlayer as balls connected with springs of natural length, b, equal to the lattice constant of the film material, and spring constant, k, representing the interatomic interactions within the layer. Acting on this layer is a sinusoidal potential, whose period, a, reflects the lattice constant of the substrate, and amplitude, V, mimics the substrate−overlayer inter-

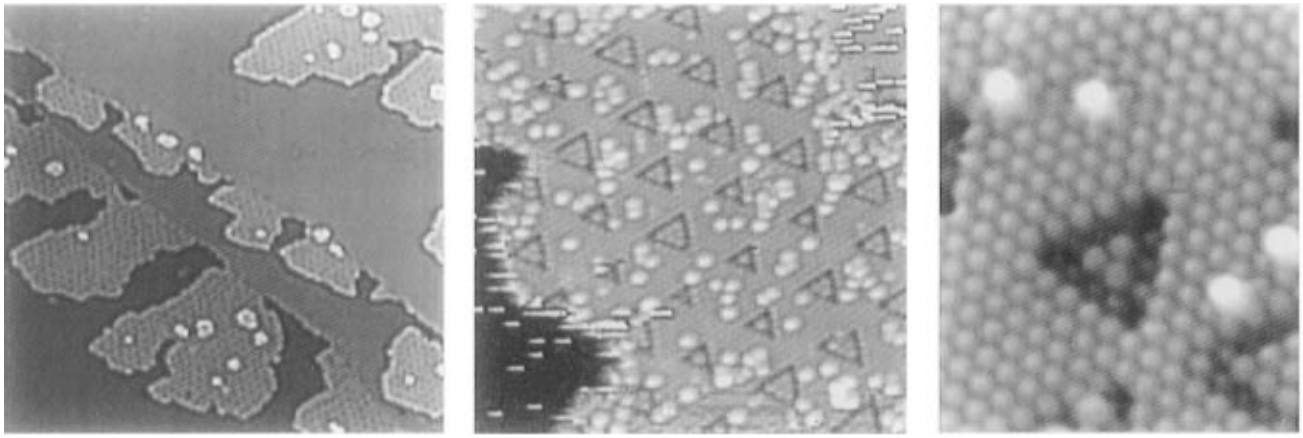

Figure 14. STM topographs of the Ni(111) surface after evaporation of Au at 300 K showing (a, top) (1450 × 1570 Å^2) 1 ML thick Au islands growing out of Ni step edges, (b, middle) (145 × 160 Å^2) the triangular superstructure in the Au layer, and (c, bottom) the atomic details of the superstructure. (Reprinted from ref 68. Copyright 1995 American Institute of Physics.)

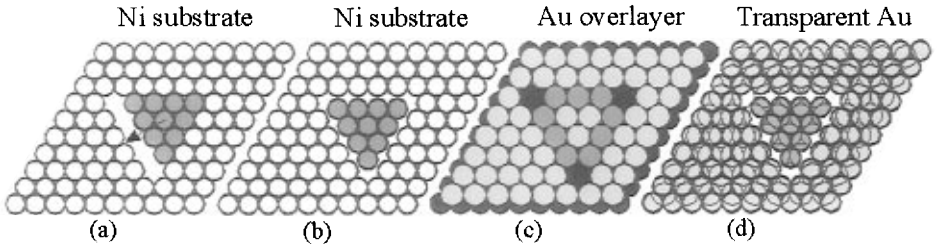

Figure 15. Hard ball model of the triangular Au−Ni(111) superstructure shown in Figure 14, illustrating the development of the misfit dislocation loops in the underlying Ni(111) surface layer. In a, five Ni atoms are squeezed out inducing the Ni atoms in the triangular area to shift by a partial lattice constant, thus creating a stacking fault and a vacancy dislocation loop b. The Au layer on top of this Ni structure (c) has the Au atoms along the edges and in the corners of the triangular structure at different heights. This results in the superstructure seen in Figure 14. (Reprinted from F. Besenbacher *Rep. Prog. Phys.* **1996**, *59*, 1737. Copyright 1996 American Institute of Physics.)

action strength. The Hamiltonian of this model can be written as

$$E = \sum_n \frac{1}{2}k(x_{n+1} - x_n - b)^2 + V\left(1 - \cos\frac{2\pi}{a}x_n\right) \quad (2)$$

where the sum runs over all atomic positions, x_n. Qualitatively, it is easy to see that the structure of the overlayer will depend on the size of k relative to V. For $k/V \gg 1$, the energy is minimized by simply allowing the overlayer to maintain its natural lattice constant. On the other hand, for $k/V \ll 1$, the lowest energy configuration is one in which the overlayer is pseudomorphic to the substrate. In the region between these two extremes dislocations appear. Ramifications of this model have been extensively tested. For the case of Cu on Ru(0001), Hamilton et al.[67] extended this model to 2D, simulating the structures of the different film thicknesses by varying the ratio k/V. They were able to show that the sequence of observed dislocation patterns can be completely reproduced with this intuitively simple model of strain relief.

Another important conclusion can be drawn from the Cu on Ru(0001) data, from the feature that, with each subsequent layer, the structure and symmetry of the surface changed. This implies that the underlying layers are being restructured as they are covered, and that the dislocations remain at the Cu−Ru interface. However, this is not necessarily the general case as shown by Jacobsen et al.[68] in their study of the growth of Au on Ni(111). For this very large compressively mismatched system (Au having a 16% larger lattice constant than Ni), the first layer is not even pseudomorphic. Instead, a trigonal trough pattern is found in the structure of one monolayer Au islands shown in Figure 14. Au triangular clusters of varying size are found in the centers of these depressions. Upon closer inspection, one finds that the atoms within the troughs are in perfect registry with the rest of the Au layer. The origin of this structure is the fact that the stacking fault is not in the Au layer, but in the topmost Ni layer. This is shown in the series of schematics of Figure 15. A triangular stacking fault surrounded by partial dislocations forms in the top Ni layer, which is then subsequently covered by Au. These partial dislocations relieve the compressive strain by locally reducing the density of the top Ni layer. The depressions in the Au layer are due to Au atoms residing above these dilute dislocations where there is more space for them to sink into the surface. Ni atoms must be ejected from the top layer in order to form these dislocation loops. They are incorporated into the Au layer and appear as the white protrusions in Figure 14. Corroborating this picture is the observation that there is a simple correspondence between the density of ejected Ni atoms and the number and size of dislocation loops.

The atomic buckling observed at partial dislocations has been attributed to the low symmetry stacking in these areas. Atoms in bridgelike sites

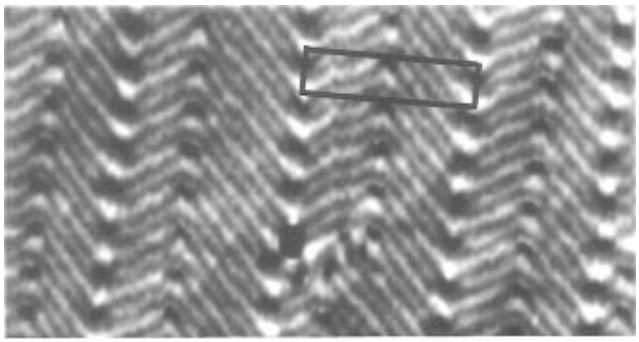

Figure 16. A 600 × 600 Å^2 STM image of a single monolayer Ag film on Ru(0001). Note the alternating lighter and darker stripes. (Reprinted from ref 63. Copyright 1995 American Institute of Physics.)

are often thought to be raised relative to those in 3-fold hollow sites from hard-sphere considerations. However, several studies have shown that this need not be the case. For example, a striped dislocation pattern is found for a monolayer film of Ag on Ru(0001)[63] which closely resembles that of the second layer of Cu on Ru(0001) as shown in Figure 16. One important difference between the two structures is that instead of the darker regions alternating in corrugation amplitude and width, it is the brighter stripes that show this characteristic. Contrary to the example of Cu/Ru(0001), these brighter areas are indeed the regions of fcc and hcp occupation accounting for the observed alternation in the bright stripes. This results in an inverted buckling of the surface as compared to a hard-sphere picture. This conclusion was corroborated by embedded atom calculations of the dislocation structure in Figure 17, which shows that the source of the inverted buckling is due to relaxations of the film and the near surface substrate. This buckling can be understood by considering a general picture of surface relaxation and thin film strain. In the area where Ag atoms occupy hollow sites, they are compressed by 6.7% relative to their bulk spacing. In the dislocation regions where the Ag atoms occupy bridge sites, the local spacing must be larger in order to compensate for the compression in the hollow site areas. The observed buckling is the response of both the overlayer and the substrate to reach a more favorable coordination for the Ag atoms in these different areas. In the bridge sites, the Ag atoms are deficiently coordinated because they have a larger lateral spacing and they are only 2-fold coordinated with the substrate. The response of the system is to enhance their coordination by shortening bond distances between neighboring Ag atoms and those between Ag and higher order Ru neighbors. This is achieved by two effects: The overlayer relaxes toward the surface and the surface bows inward to "cup" the Ag (see Figure 17b). In complementary fashion, the Ag atoms residing in hollow sites are over-coordinated, their neighbors being compressed. In order to reduce this coordination state, the system locally relaxes outward, bowing the surface. Similar buckling phenomena have been observed by STM in Au on Ni(111),[68] Pb on Cu(111),[69] and Ag on Cu(111).[70,71]

The formation of close-packed stacking faults is in fact an energetically efficient path to strain relief in other film orientations as well. Müller et al.[72,73]

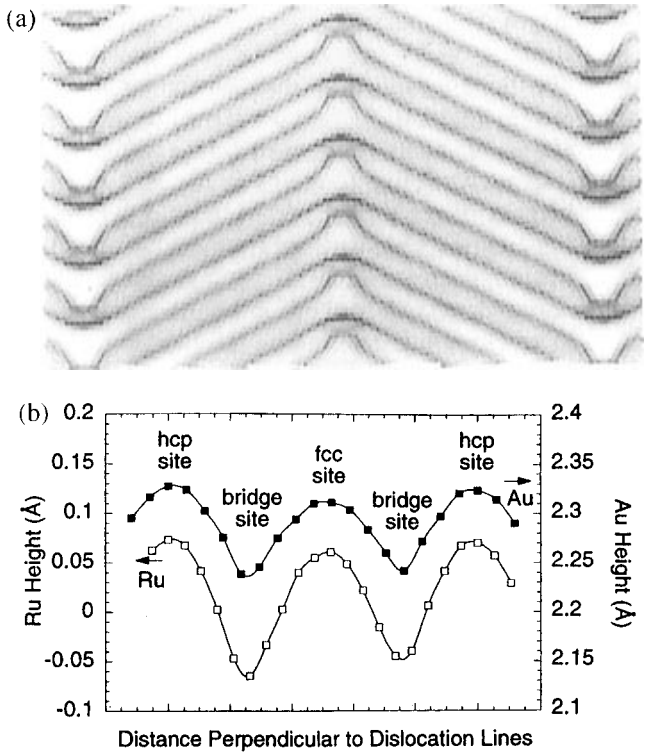

Figure 17. (a) Gray-scale image of Ag atom heights from EAM calculation. The area is 280 Å × 168 Å. The gray-scale range is 0.16 Å. (b) Plot of Ag atom heights from EAM calculation. The height of the top layer of Ru atoms is also plotted. Strains due to the Ag−Ru mismatch cause the Ru substrate to buckle. This buckling attenuates over a depth of about 10 layers into the Ru. The buckling causes the reversal of the expected relative heights of hollow and bridge sites for the Ag overlayer. (Reprinted from ref 63. Copyright 1995 American Institute of Physics.)

recently investigated the strain relief mechanisms for Cu layers on Ni(100). Similar to the (111) case, linear stripes of surface buckling were observed by STM. With increasing thickness, the width of the stripes grew as can be seen in Figure 18. This is consistent with the fact that these stripes are due to the formation of stacking fault regions on buried (111) planes in the Cu overlayer which the authors term "internal (111) faceting". The model is schematically shown in Figure 19 for one to three layers of Cu. The stacking fault begins in the first layer by a lateral shift of one Cu row to bridge sites on the Ni. This causes the narrow stripe observed in the first layer. With subsequent layers, wider regions of buckling occur due to stacking on nearest-neighbor sites of the original stripes. By three layers, one can readily see that this initial shift of the first layer leads to stacking faults along internal (111) planes. So again the strain relief occurs through the formation of energetically favorable (111) stacking faults. This model is further substantiated by the fact that the stripes were never observed to cross or coalesce as would be geometrically disallowed. Furthermore, the width of the stripes was measured to increase linearly with layer thickness while the density of stripes remained nearly constant, as implied by the model.

It is not only the structure of dislocation networks that is important to the properties of thin films. Their dynamics are crucial in determining the mechanical properties. STM is proving valuable in this area by allowing time-resolved imaging of the film

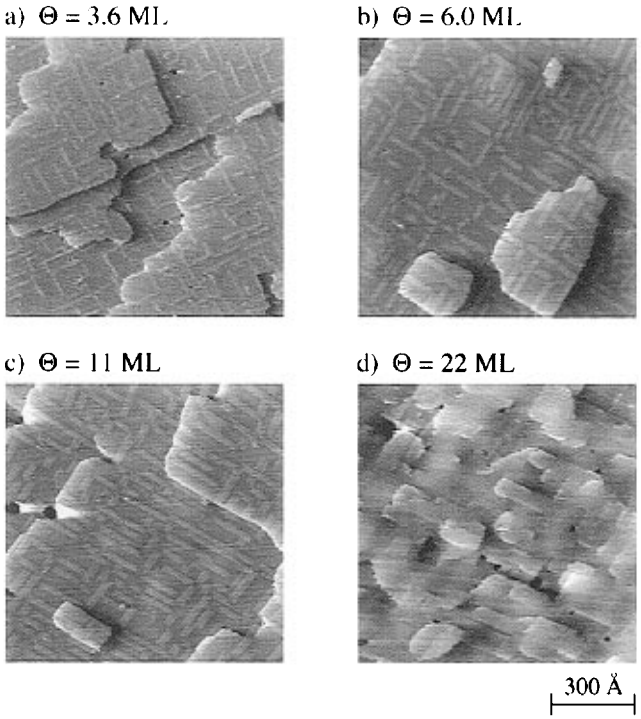

Figure 18. STM images of Cu multilayer films on Ni-(100): (a) 3.6 ML, (b) 6 ML, (c) 11 ML, and (d) 22 ML. (Reprinted from ref 72. Copyright 1996 American Institute of Physics.)

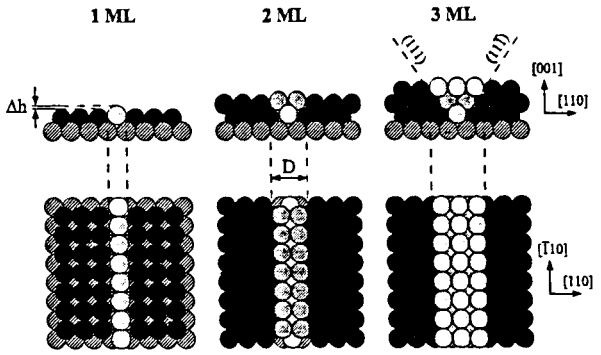

Figure 19. Schematic of the "internal (111) faceting" model describing the appearance of the stripes on the Cu/Ni(100) film. The figure shows side and top views for 1, 2, and 3 ML. The shaded circles represent the substrate atoms (Ni). The "dark atoms" (Cu) are placed at the 4-fold hollow sites in the pseudomorphic geometry. The "light atoms" (Cu) form the stripes and are placed at the 2-fold bridge sites in the first layer. As indicated in the 3 ML schematic, this forms (111) stacking faults along the stripes. (Reprinted from ref 72. Copyright 1996 American Institute of Physics.)

structure. As an example, we consider the dynamics of dislocations in the first layer of Cu on Ru(0001) at room temperature.[74] Although the equilibrium structure of the complete first layer is pseudomorphic as described above, dislocations in the first layer form in the presence of a partial second layer. Figure 20 shows partial dislocations in the second layer continuing past the edge of the second layer island, and forming intersections in the first layer. At such intersections are the cores of perfect edge dislocations where an extra row of atoms terminates. The results of embedded atom method calculations of the atomic structure of such a loop are shown in Figure 21, indicating the partial extra row of atoms. By imaging

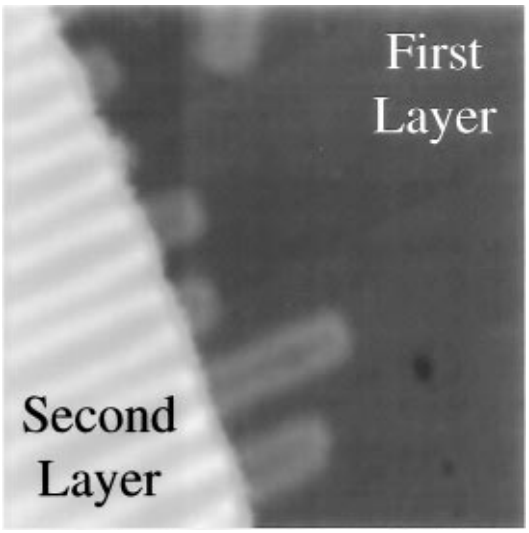

Figure 20. Room temperature STM image (270 × 270 Å^2) of a Cu film on Ru(0001) exposing regions of one (dark) and two (bright) atomic layers. Partial dislocations are imaged as bright stripes forming an ordered array perpendicular to the step in the second Cu layer. Partial dislocations in the first layer emerge where second layer dislocations reach the step edge. (Reprinted from ref 74. Copyright 1997 American Institute of Physics.)

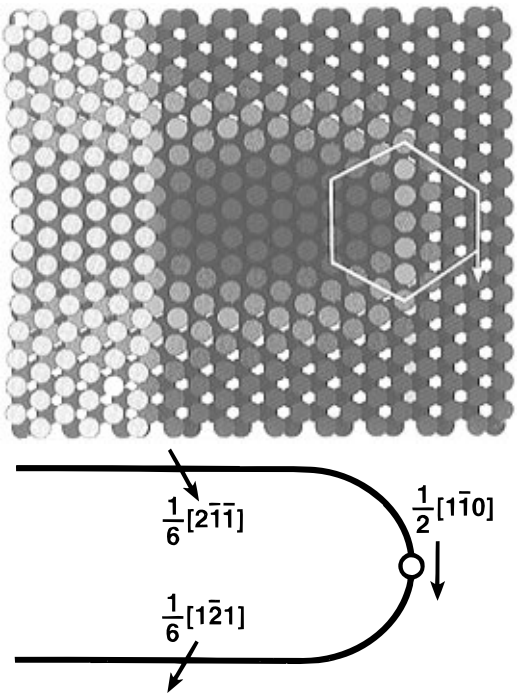

Figure 21. Dislocation structure at a second layer step edge, calculated using embedded atom potentials. A Burgers circuit is superimposed to indicate the perfect edge threading dislocation that forms at the intersection of the two partial dislocations. (Reprinted from ref 74. Copyright 1997 American Institute of Physics.)

this structure as a function of time, Schmid et al. found them to fluctuate in length.[74] This is shown in the sequence of images of Figure 22. In order for this motion to occur, atoms must be added or removed from the extra row, a process known as dislocation climb. It is the equilibrium Cu adatom gas on the surface of the film which acts as the source and sink of these atoms. To further understand and quantify the dynamics of this process, temporal correlations in the dislocation motion were measured (see Figure

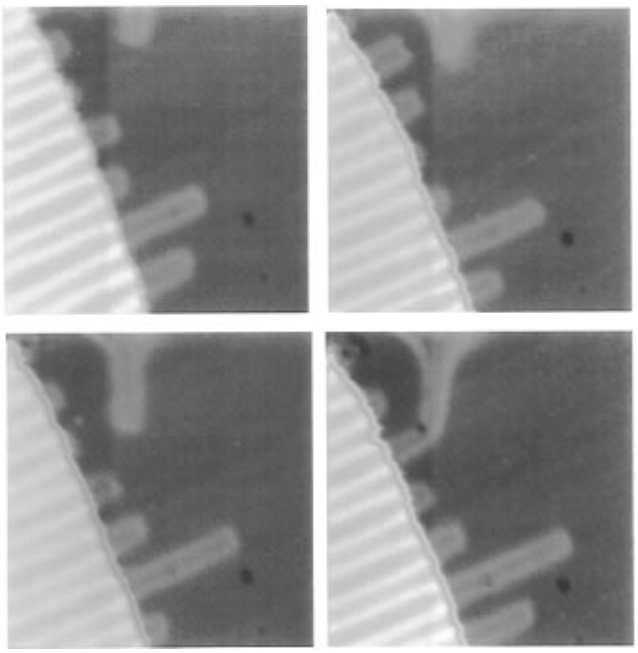

Figure 22. Time sequence of motion of dislocations in the first layer of Cu on Ru(0001) at room temperature. Images (270 × 270 Å^2) were acquired 30 s apart (clockwise from the upper left). Motion can be referenced to the stationary impurity (black dot) in the lower right of the image. (Reprinted from ref 74. Copyright 1997 American Institute of Physics.)

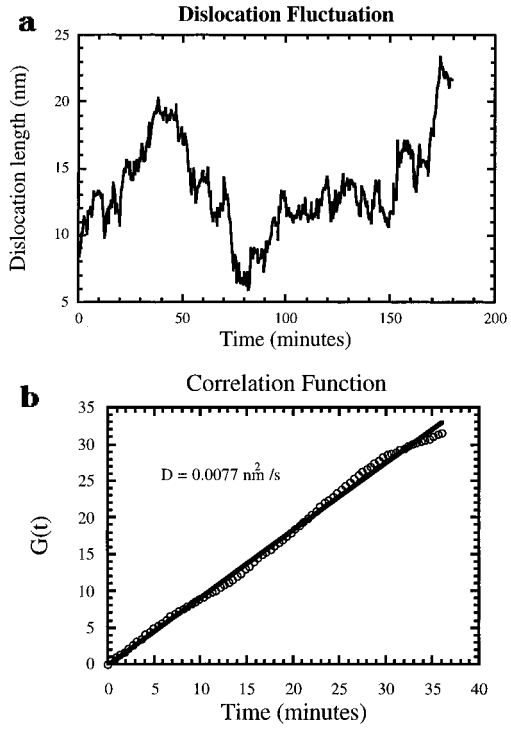

Figure 23. (a) Trajectory of the end of an edge dislocation in the first layer of Cu on Ru(0001), over a 3 h period. Data were obtained from 270 × 270 Å^2 images, at 27 s intervals. (b) Corresponding time dependence of the mean-square displacement. Circles (triangles) are from 30 nm^2 (350 nm^2) images acquired every 27 s (10 min). (Reprinted from ref 74. Copyright 1997 American Institute of Physics.)

23a). The correlation function for this motion is linear (Figure 23b) in time, indicating that these fluctuations can be described by simple 1D random walks (for not too short lengths). The diffusion rate

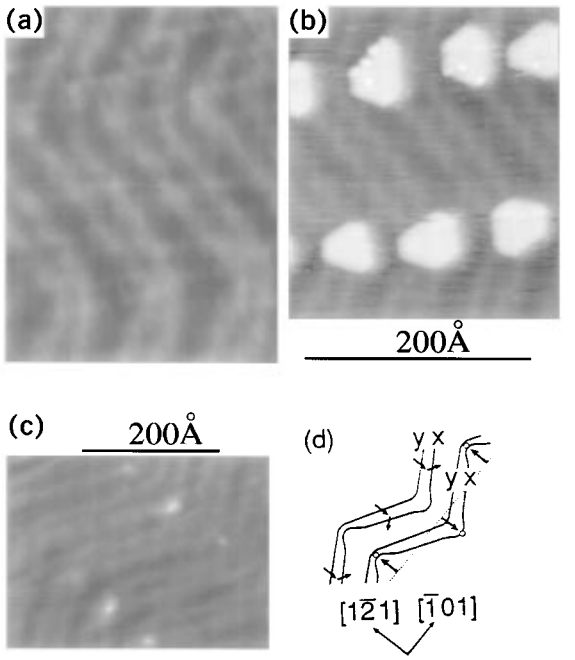

Figure 24. Correlation of Ni island nucleation with Au reconstruction. (a) Typical reconstructed section of large terrace on clean Au(111). Light zigzagging bands are ~0.2 Å high ridges where atoms are near bridge sites. "Elbows" in ridges lie on two nearly horizontal domain boundaries. The lower boundary contains "pinched" elbows; the upper one, "bulged" elbows. (b) Nucleation of polygonal shape Ni islands (coverage 0.14 ML; deposition rate 0.1 ML/min). Of thousands of islands observed in dozens of STM images that reveal both islands and reconstruction ridges, ~99% form at these elbow sites. In b and c a nonlinear scale is used to make ridges visible. (c) Nucleation of Ni islands at elbows (coverage 0.1 ML; deposition rate 0.05 ML/min). Three islands are seen on each of two domain boundaries of the herringbone pattern, running diagonally from upper left to lower right. (d) Sketch of herringbone pattern and nucleation sites. Two pairs of ridges are shown as dark bands. Arrows on the upper pair show directions of Burgers vectors. On the lower pair, small circles mark island sites (cf. panel c), located symmetrically about the central axis of the ridge (dashed line). (Reprinted from ref 75. Copyright 1991 American Institute of Physics.)

of 0.008 nm^2/s is given by the slope of the correlation function. From this, the net exchange rate between the adatom gas and the dislocations was estimated to occur at a rate of one atomic exchange every 30 s.

Finally, it should not be surprising that there is an intricate relationship between film dislocation structure and island nucleation and growth. Dislocation patterns are inhomogeneities in the surface that can alter many of the atomistic processes involved in island nucleation and growth. For example, binding and diffusion at and across dislocations differ substantially from those on a perfect surface. STM provides an exceptional method for investigating this behavior because of the ability to locally image islands and the surrounding surface structure. An excellent example of this is the work of Chambliss et al.[75,76] on the initial stages of nucleation of Ni islands on the reconstructed surface of Au(111). The surface layer of Au(111) is known to laterally contract by 4%. This contraction is achieved through formation of domains of linear partial dislocations, in an alternating fashion known as the herringbone pattern (Figure 24a). At every other elbow of this structure, the partial dislocations meet to form

perfect edge dislocations. Chambliss et al.[75,76] found that nucleation of Ni islands occurs preferentially at the cores of these dislocations, i.e., where the extra row of atoms terminates and the Au lattice is highly distorted. This leads to the formation of an array of nanometer scale Ni islands as shown in Figure 24. This same phenomenon was found also for Co[77] and Fe[78] on Au(111).

IV. Composition and Alloying

The integrity of thin film interfaces determines to a large extent its electronic and magnetic properties. Thus the degree of alloying between adlayer and substrate at the initial stages of deposition is of fundamental interest. Of course, bulk phase diagrams of alloys have been compiled for numerous binary and ternary systems, but a question remains as to how applicable this information is in a thin film situation where interface strain and reduced dimensionality can make the systems far from bulklike. The application of STM to these problems has recently surged, primarily due to the recognition of the ability of STM to resolve different atomic species within the same layer.[79] In the two previous sections, the influence of forming a film−substrate interface on the total free energy of the system included growth mode determination and dislocation formation. Another important process that can minimize the total free energy is modification of the composition of the film−substrate interface. Rich alloying behavior has been discovered ranging from expected results, as in the case of alloys mimicking stoichiometries of known bulk phases, to completely new thin film alloys formed from bulk immiscible metals. Several examples of each type of behavior are presented below.

A number of groups have studied the growth of metals onto substrates for which alloy formation is known to occur in the bulk (Au/Ag(110),[80,81] Ni/Au(111),[75,82,83] Au/Cu(100),[75,82,83] Rh/Ag(100),[84] Ag/Pt(111),[85] Pd/Cu(100)[86]). In some cases, stable ordered surface structures are observed that are related to an ordered bulk phase. This is the case of Au deposited on Cu(100). Chambliss et al.[82,83] found that in the range of 0.1 to 0.5 ML, a c(2×2) pattern is formed that closely resembles the (100) face of the bulk Cu_3Au alloy.[87,88] This structure exists in the exposed substrate surface as well as in monolayer islands that were nucleated on terraces. Atomic resolution images of this structure are shown in Figure 25, along with a superimposed model for the positions of the Au and Cu atoms. The corrugation difference between the two species was found to be about 0.2 Å, which agrees with the estimated Au−Cu height difference. The formation of this alloy structure is possibly due to Au exchanging with surface Cu (the latter having higher surface free energy) thereby becoming incorporated into the surface. (Exchange processes are known to exist and be the primary mechanism of adatom diffusion on many surfaces.[2]) This has the simultaneous effect of supplying Cu adatoms to form the alloy structure in the top layer islands. Remarkably, this alloy is confined only to the first layer, thus the term surface alloy. One consequence of this is that the "substrate" of this alloy is Cu(100) which has a smaller lattice constant than bulk Cu_3Au. To accommodate this strain, "nanometer faults" appear by shifting linear atomic rows to form closer packing with nearest-neighbor rows as shown in Figure 25. This is structurally similar to the strain relief mechanism found for Cu on Ni(100) discussed in the previous section. The same type of ordering has been found in several other systems on fcc(100) surfaces (Pd/Cu(100),[89] Mn/Cu(100)[90]). Similar effects were seen in the formation of a stoichiometric $NaAu_2$ surface alloy on Au(111).[91] Despite the appeal of extrapolating the stoichiometries of bulk alloys to predict alloying behavior at the surface of thin films, many new and unexpected surface alloying phenomena are likely to be discovered. For example, in the case of a mixture of Ag−Pt, where several stable stoichiometric alloy phases are known to exist, Röder et al.[85] found that deposition of Ag on Pt(111) leads to a surface confined alloy consisting of Ag clusters in the size range of 7−12 atoms dispersed in the top Pt(111) layer.

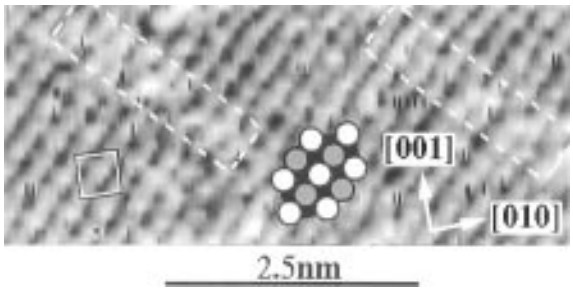

Figure 25. Atomic resolution image of the c(2×2) structure of the Cu_3Au alloy (in the superimposed array white circles are Au and gray circles are Cu). The small square marks a single c(2×2) unit cell (0.36 nm^2) with one higher atom (presumably Au) at the center. The dashed-line rectangles contain regions of disrupted atomic positions associated with "nanometer faults" along the [011] direction. (Reprinted from ref 75. Copyright 1991 American Institute of Physics.)

The formation of an interface alloy can also change relative surface and interface energies, thus potentially altering observed growth modes. For example, Au has been reported to grow layer-by-layer on Ag(111) and Ag(100). However, Au deposited at room temperature on Ag(110) eventually forms 3D islands. Rousset et al.[92] discovered that the first monolayer of Au mixes with the substrate and is encapsulated by one monolayer of Ag. A model of this structure is shown in Figure 26. This occurs because the more open structure of the (110) surface provides a low-energy pathway for Au−Ag atomic exchange. Surprisingly, after one monolayer, intermixing stops. Apparently, the strong Au−Ag bonds formed in this mixed layer inhibit further interdiffusion at room temperature. Instead, additionally deposited Au forms 3D islands on top of this intermixed layer, suggesting that this surface alloy has low enough surface free energy to the point of inducing Stranski−Krastanov growth.

Encapsulating behavior driven by a surface free energy reduction has also been found in immiscible systems. Co films on Cu(100)[93] and Cu(111)[94] have been observed to be capped by diffusing Cu atoms to form a Cu/Co/Cu sandwich structure. Cu has a substantially lower surface free energy of 1.9 J/m^2, compared to 2.7 J/m^2 for Co. On the Cu(111) substrate, the Co islands grow as bilayers which are then capped by Cu.[94] On the Cu(100) surface, annealing of a Co film leads to substantial smoothing of the

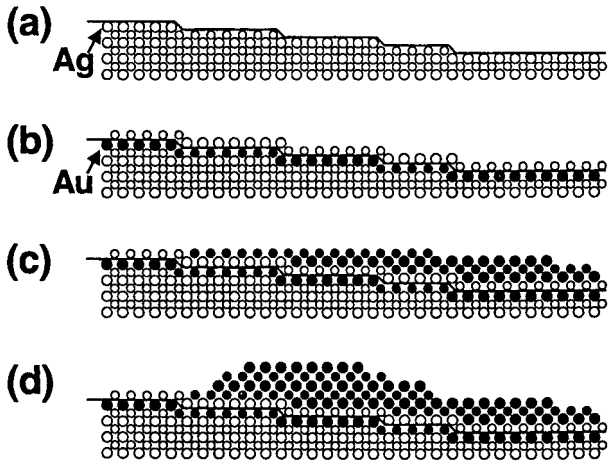

Figure 26. Schematic showing stages of "intermixed Stranski−Krastanov" growth for Au/Ag(110). Filled (open) circles indicate Au (Ag) atoms. Two circle sizes denote atoms in different vertical (001) planes: (a) Clean Ag(110), with line showing initial step positions; (b) ~1 ML Au on Ag(110), with nearly all Au atoms underneath the top layer of Ag; (c) 2D finger growth of Au on top of the intermixed layer. (d) further growth leads to 3D islands. (Reprinted from ref 81. Copyright 1994 American Vacuum Society.)

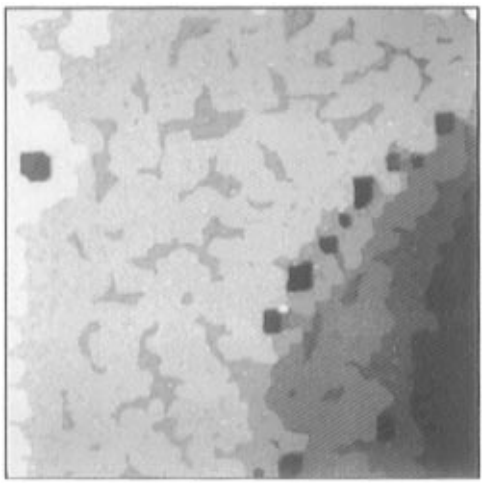

Figure 27. A 150 × 150 nm^2 image of a 3.2 ML Co/Cu(100) film annealed for 1000 s at 490 K. Pits (black rectangular features) reaching deep into the Cu(001) substrate form predominantly in a step band which was already present on the Cu(100) substrate before film preparation. (Reprinted from ref 93. Copyright 1993 American Institute of Physics.)

surface and the formation of rectangular pits much deeper than the thickness of the film.[93] This is shown in Figure 27 for a 3.2 ML Co film after annealing to 490 K for 1000 s. From spectroscopy measurements, it was concluded that the annealing resulted in a one monolayer capping of the Co film. It is this migration of Cu to the surface that leads to pit formation (cf. ref 95 for the case of Fe/Cu(100)). The walls of the pits are the four equivalent (111) facets of the Cu crystal. This faceting greatly enhances the transfer of Cu to the surface since the diffusion of adatoms on closed-pack surfaces is faster. This annealed configuration is somewhat surprising because simple surface energetic considerations would predict that the lowest energy structure would be 3D Co islands exposing Cu(100) surface area. The reason this does not occur is due to kinetics. The fast Cu diffusion on Cu(111) facets overwhelms the Co mobility that is necessary for Co cluster formation. Encapsulation has also been found for Cu deposited on Pb(111).[96] The large difference in the surface free energies between Cu and Pb (1.9 J/m^2 compared to 0.5 J/m^2, respectively) leads to 3D island growth. However, the rapid diffusion of Pb leads to complete encapsulation of the Cu clusters by a single monolayer of Pb on the surface as shown in Figure 28.

The most fundamentally surprising result recently found is that immiscible combinations of metals can lead to alloy formation at surfaces. This was first observed by Chambliss et al. for Fe on Cu(100).[97−99] Despite limited miscibility of these two metals, Fe atoms are found to exchange places with Cu atoms in the surface layer and form clusters of incorporated Fe and first layer islands of mixed Cu−Fe. This phenomenon has been recently examined in detail for Au on Ni(110).[75,100] Like Fe/Cu(100), upon room temperature deposition of Au, place exchange occurs with substrate Ni atoms, resulting in the incorporation of the Au atoms into the surface and the formation of Ni chains in the [1$\bar{1}$0] direction (Figure 29). To understand the origin of this mixing of immiscible metals, calculations using EMT were performed to obtain the minimum energy structures of Au on and in the Ni(110) surface. The results point to the following picture. Ni atoms in the (110) surface have a coordination number of 7 which is much smaller than the ideal bulk coordination of 12. Because the Au electron density is more extended than that of Ni, an incorporated Au atom in the surface will increase the effective coordination of more Ni atoms than a Au adatom would. Thus the total surface energy is lowered by surface alloy formation. Furthermore, the calculations showed that the ideal number of Ni atoms surrounding a Au atom is 8, which is much closer to the number of Ni nearest neighbors in the surface layer, 7, as compared to Ni on the surface, 5, or in the bulk, 12. Thus, interestingly, this alloy phase is only stabilized at the surface. With increasing Au coverage, the compressive stress induced in the surface increases to a point where Au atoms are squeezed out, effectively dealloying the surface.[100] Very similar effects were found for Pb on Cu(111).

A framework for understanding these phenomena was developed by Tersoff.[101] Consider a thin-film system of lattice mismatched and bulk immiscible materials A grown on substrate B. The fact that they are bulk immiscible implies that there is an energy cost for creating A−B interfaces. Thus in the bulk, the two materials phase segregate to minimize A−B interactions. In a lattice mismatched film system, minimizing A−B interactions leads to a perfectly sharp interface, but then the mismatch leads to a positive strain energy. Tersoff considered the possibility that an energetically more favorable configuration could be reached through intermixing: reducing strain energy at the cost of interface energy. To investigate this possibility, strain energy was calculated using the pairwise Keating model:[102]

$$E_{\text{strain}} = \alpha \sum_{ij} (r_{ij}^{\,2} - b_i b_j)^2 \qquad (3)$$

where r_{ij} is the distance between atoms i and j, and the sum is over nearest-neighbor pairs only. The preferred bond length of atom i is b_i, and the bond

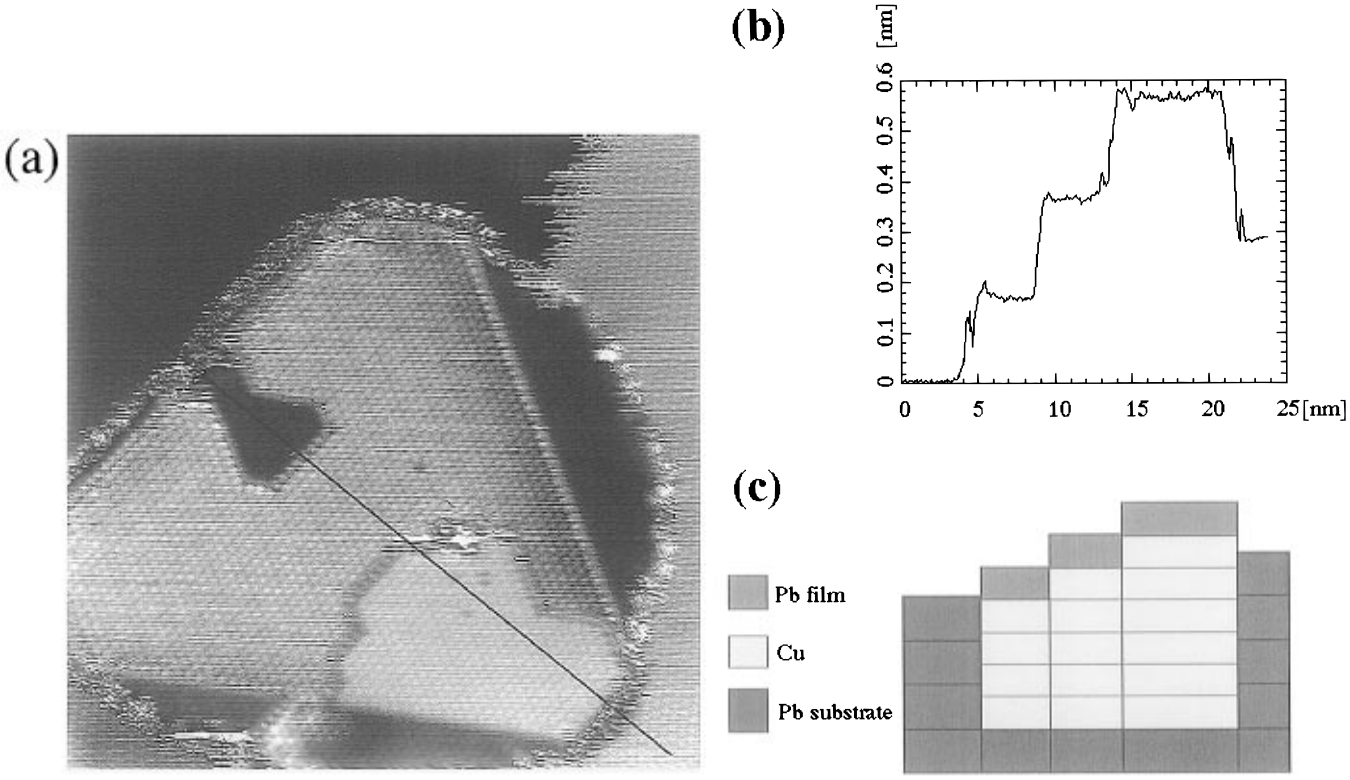

Figure 28. (a) A 20 × 20 nm^2 STM image of a Cu island on Pb(111). The lattice of the Pb overlayer as well as the Cu island lattice is rotated by 30° with respect to the Pb substrate. The Pb overlayer exhibits the moiré pattern of Pb on Cu(111). This image was slightly differentiated, and the height difference between various terraces reduced. (b) Section through a marked by the line. (c) Model for the Cu island that best fits the section in b. Each rectangle represents a single layer. (Reprinted from ref 96. Copyright 1995 American Institute of Physics.)

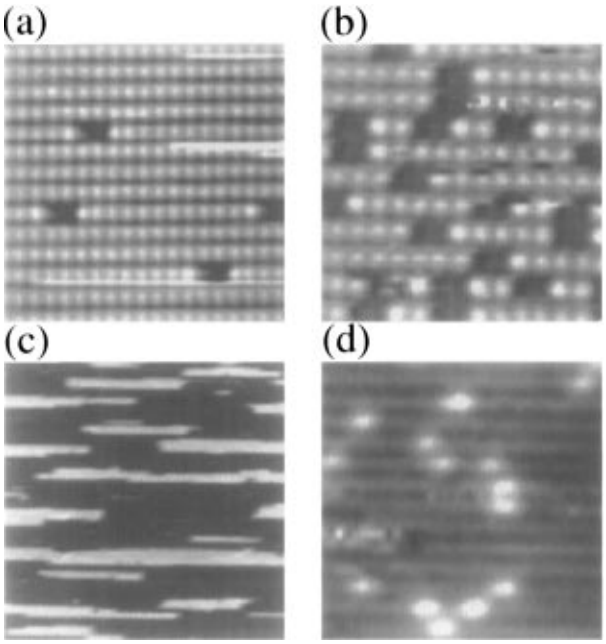

Figure 29. Atomically resolved STM topographs (36 × 38 Å^2) at Au coverages of (a) 0.05 ML, (b) 0.35 ML, and (d) after a tip change where the holes are transformed into protrusions (~0.15 Å) along the [1$\bar{1}$0] direction (0.18 ML). In b, a Ni(1×1) mesh is superimposed, and in a, the corrugations along the [1$\bar{1}$0] and [001] directions are 0.02 and 0.10 Å, respectively. (c) STM topograph over a large area (702 × 765 Å^2) at a coverage of 0.17 ML showing the anisotropic growth of 2D Ni islands. The gray scale is such that protrusions are white, while depressions are black. (Reprinted from ref 100. Copyright 1995 American Institute of Physics.)

stiffness is α. Note that in the small displacement limit, this reduces to a Hooke-type interaction. Choosing the lattice constants of A = Au and B = Ni and making an appropriate choice of α to reproduce the bulk elastic constants of Ni and modulus of Au, minimization of strain energy clearly favored Au in the surface layer as opposed to in the bulk, due to the greater possibility for strain relaxation at the surface. To include the effect of a finite interface energy, an amount Δ_{AB} of energy was added to each A−B bond. For a segregating system, Δ_{AB} is positive. Through Monte Carlo simulations for various values of Δ_{AB} greater than or equal to zero, the tendency for A clustering within a B layer can be evaluated. The results of these simulations are summarized in Figure 30. For no interface energy ($\Delta_{AB} = 0$), the Au atoms are dispersed throughout the layer to minimize strain. As the interface energy increases, more clustering occurs to reduce the total interface length at the cost of increased strain.

Alloying effects are expected to play an important role in the technologically relevant field of metallic superlattices. Stevens et al. have taken the first step at studying such systems by investigating alloying in bimetallic films.[103] As a model system, Cu−Ag films on Ru(0001) were examined. This group of surface metals and substrate was chosen because they are all mutually immiscible. Furthermore, the role of strain is controlled by their relative lattice constants in the close-packed plane; $a_{Cu} = 2.55$ Å, $a_{Ru} = 2.71$ Å, and $a_{Ag} = 2.88$ Å. Thus, for example, one expects that an alloy of Cu−Ag would have a lattice constant much closer to that of the substrate

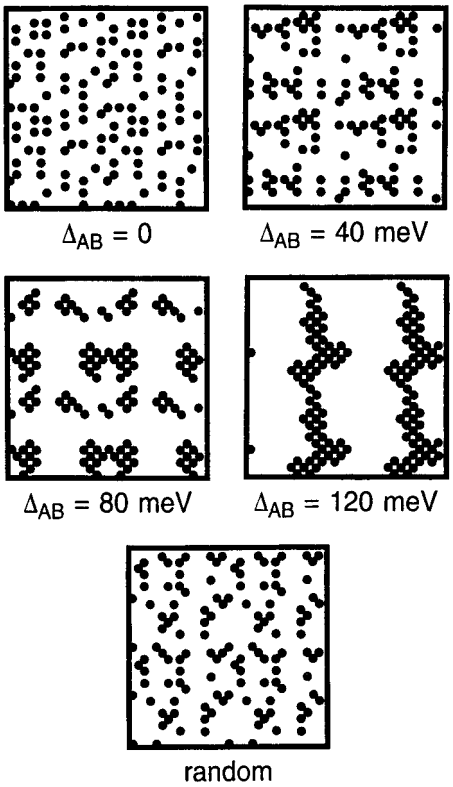

Figure 30. Distribution of Au atoms within the surface layer. Results are shown for four indicated values of Δ_{AB}, the energy cost per A−B bond. A random distribution is shown for comparison. Each image corresponds to four unit cells, periodically repeated for visual clarity. The dot size is chosen to just touch for neighboring atoms. (Reprinted from ref 101. Copyright 1995 American Institute of Physics.)

than either Cu or Ag alone. (Previous studies of deposition of the individual metals on Ru(0001) indicated that no alloying with the substrate occurs.) Thermal desorption studies of both Cu and Ag on Ru(0001) have indeed indicated that they desorb from a mixed Ag−Cu phase. The STM results confirm this conclusion. Triangular domains of a stoichiometric 2D alloy form on the surface, separated by regions of pure Ag (Figure 31). This domain structure exposes the intimate relationship between the alloy formation and strain relief. The two triangular orientations represent the alloy in the two types of pseudomorphic stacking, fcc and hcp. Furthermore, the stripes of Ag separating them are in fact partial dislocations. As the Cu concentration is increased from this composition, the alloy domains become larger at the expense of the total length of partial dislocations, until a uniform stoichiometric alloy covers the surface.

The atomic processes of alloy formation or interdiffusion within bimetallic films are expected to be very different than those of alloying between a film and substrate because the intralayer alloying may not involve direct exchange with the substrate. Schmid et al. investigated this issue for the case of Co−Cu on Ru(0001)[104] where previous studies have shown that neither Co nor Cu alloy with the Ru(0001) substrate. The approach taken was to mimic the traditional interdiffusion technique of forming a sharp interface and then measure the concentration profiles across this interface as a function of time at

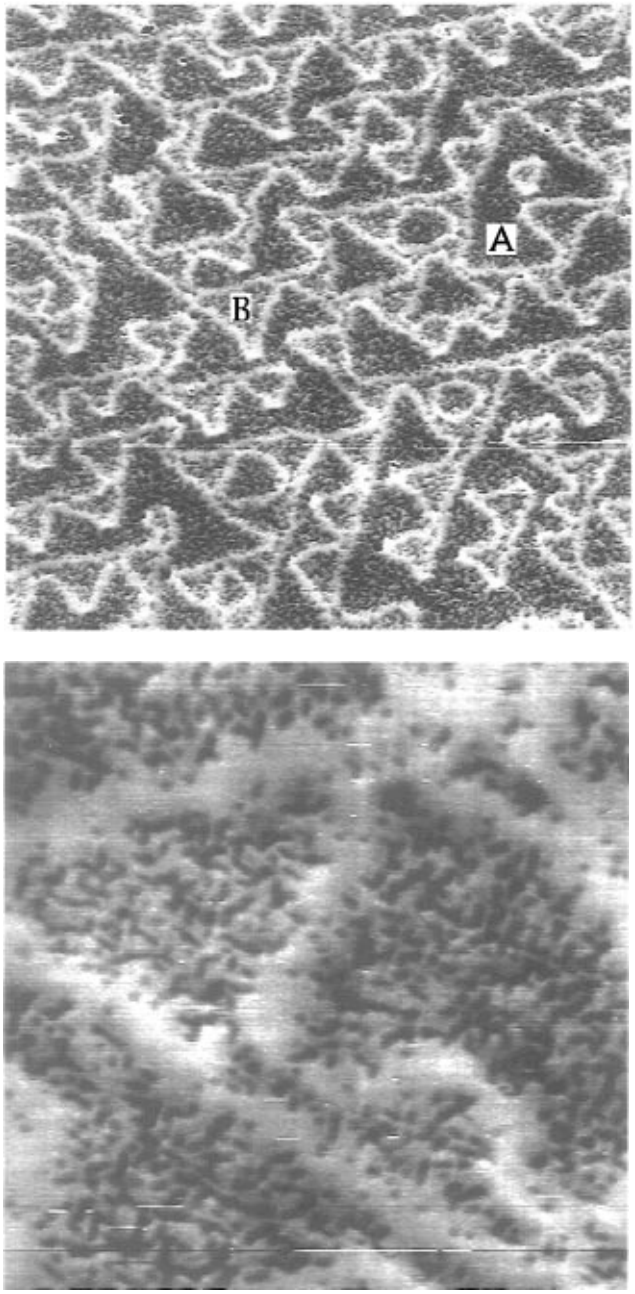

Figure 31. (a, top) 1000×1000 Å^2 image of film with $X_{Cu}/X_{Ag} = 0.42$ following annealing to 550 °C. Two domains of the alloy can be seen and are separated by domain walls made up of the pure Ag phase. Details of the alloy domain structure and domain walls can be seen in b (bottom) (200 × 200 Å^2). (Reprinted from ref 103. Copyright 1995 American Institute of Physics.)

a specified temperature. In this case, however, the interface is one atomic layer high and linear. STM images of a Cu−Co interface on Ru(0001) after different amounts of annealing are shown in Figure 32. Important here is that each image is of precisely the same interface. From this data, concentration profiles could be extracted as plotted in Figure 33. For traditional bulk interdiffusion, vacancy or interstitial diffusion is the dominant mechanism and therefore is governed by the solution of Fick's law of diffusion, leading to an error function profile. This is clearly not the case here as is indicated by the lack of agreement between the error function and the measured profile (inset of Figure 33). The difference

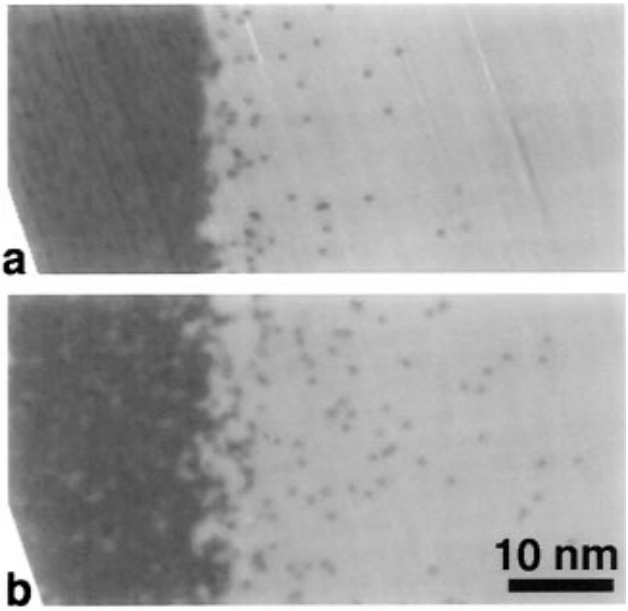

Figure 32. Early stages of interdiffusion at the one-dimensional interface between adjacent regions of one monolayer Co (left) and one monolayer Cu (right) following 580 K annealing for 1 min (a) and 5 min (b). (Reprinted from ref 104. Copyright 1996 American Institute of Physics.)

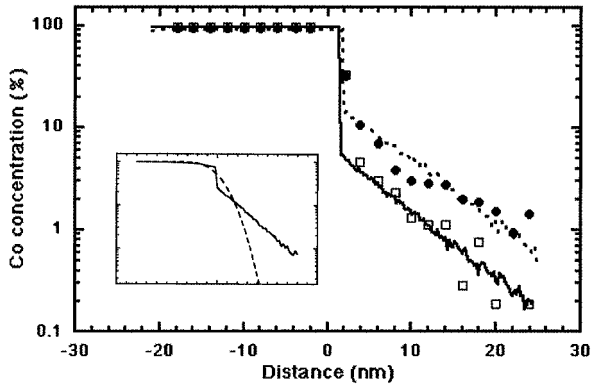

Figure 33. Co concentration profiles across Co−Cu interfaces annealed to 580 K for 1 min (open squares) and 5 min (dark circles). Simulation results are superimposed for the 1 min (solid line) and 5 min (dashed line) anneals. The inset compares a simulation profile (solid line) with the error-function form characteristic of concentration gradient driven interdiffusion (dashed line) for the same interdiffused mass. (Reprinted from ref 104. Copyright 1996 American Institute of Physics.)

is due to the existence of a 2D lattice gas on the surface which can exchange atoms with those in the film, thus mediating interdiffusion. This process acts as a short-circuit to the standard picture of vacancy driven interdiffusion and results in the observed exponential concentration profiles of Figure 33. This mechanism was confirmed by Monte Carlo modeling. The important parameter is the ratio of the exchange rate to the adatom diffusion rate. In the simulation, the 1 min data was first fitted and this ratio extracted. Then, without any other free parameters, the simulation was evolved for an additional 4 min. The results accurately reproduced the 5 min profile. The results of both simulations are superimposed on the data in Figure 33.

The kinetics of film growth can also be unconventional in the case of bimetallic films as can be seen

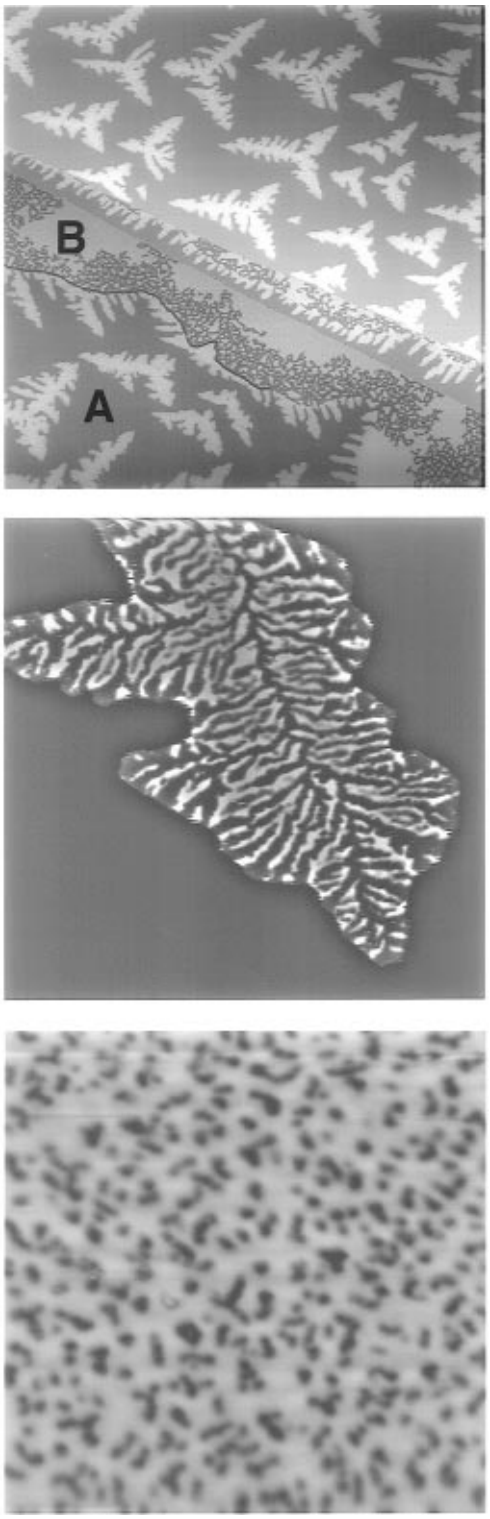

Figure 34. (a, top) A 7500 × 7500 Å^2 image of a Co−Ag alloy grown at 70 °C as described in the text. (b, middle) A 500 × 500 Å^2 image of dendritic island nucleated away from original Ag islands. (c, bottom) A 400 × 400 Å^2 image of compact islands nucleated in areas originally covered with Ag. (Reprinted from ref 105. Copyright 1996 American Institute of Physics.)

in the study of Ag−Co on Ru(0001).[105] At room temperature, dendritic islands form on the surface (Figure 34) despite the fact that neither metal grown individually on Ru(0001) produces such shapes. These islands are in fact made up of a mixture of both metals with a specific structure. Alternating veins of Ag and Co run along the primary directions of the

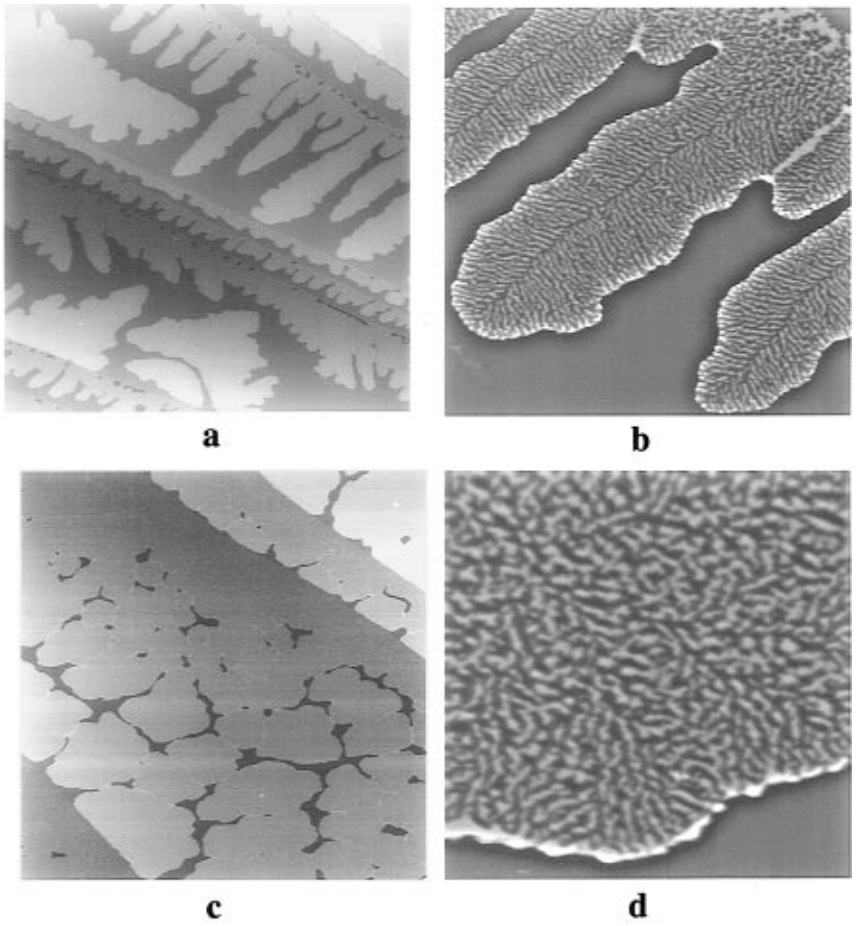

Figure 35. (a) A 6000 × 6000 Å^2 image of a Co−Ag alloy grown at 138 °C as described in text. (b) A 1750 × 1750 Å^2 image of the vein structure with the finger islands of a. The image is contrast enhanced, so that the intensity difference between the Co and Ag represents a corrugation height of about 0.2 Å. Note the integrity of the veins. (c) A 10 000 × 10 000 Å^2 image of a Co−Ag alloy grown at 170 °C. Islands now exhibit compact shapes. (d) A 600 × 600 Å^2 image of the internal structure of the islands of c. Continuous vein structure no longer exists at this growth temperature. (Reprinted from ref 105. Copyright 1996 American Institute of Physics.)

dendritic growth. The link between this internal structure and the island shapes can be seen in the series of STM images of Figure 35. Deposition at elevated temperatures continues to produce dendritic islands with the internal vein structure up to about 170 °C. Above this temperature, the dendritic shape and the internal structure simultaneously disappear. As seen in the sections above, dendritic behavior is linked to reduced edge mobility. The connection between the vein structure and the edge diffusion barriers around an alloy island can be understood schematically by considering a small Co−Ag (Co, gray, and Ag, white) cluster diagrammed in Figure 36. Also plotted is the energy diagram for a Co atom at various positions along the edge of the cluster. For diffusion along each metal individually, a small barrier is encountered due to the close-packed structure of the island edge. However, for a Co atom to cross from a Co region to a Ag region along an edge, an additional energy barrier, δ, must be crossed, which depends on the energy difference between a Co−Co bond and a Co−Ag bond. Thus it is more difficult for atoms to diffuse across these interfaces, leading to a reduced edge mobility. (A similar energy diagram exists for Ag.) In this way, kinetics favors the continued growth of like-metal species and encourages dendritic island shapes.

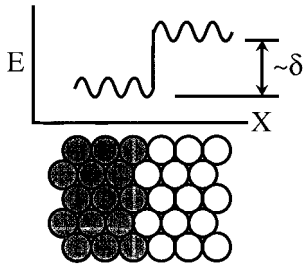

Figure 36. Schematic of the energy corrugation experienced by a Co atom at the edge of a vein structure. Ag and Co atoms are represented as white and black balls, respectively. (Reprinted from ref 105. Copyright 1996 American Institute of Physics.)

V. Conclusion

STM has proven to be an invaluable tool not only to provide information on metal film growth morphology and structure, but more importantly to fingerprint the underlying atomic processes. Prior to its implementation, a detailed understanding of how important kinetics is to determining the final outcome of a growth process could not be thoroughly investigated. The use of STM in this field has revealed that subtle differences in one or only a few atomic processes can in fact have a dramatic influence on the micrometer length scale properties of a film. We are now certain that some different metal

atoms avoid each other on the surface, while others form unexpected alloys or sandwich structures. In response to strain, they form complex dislocation structures that can move like simple random walkers on surfaces. However, the full potential of STM to provide insight into metal epitaxy has not nearly been reached. Through time-resolved STM imaging and even new techniques such at STM tracking,[106] application of STM to phenomena such as pattern formation at surface reaction fronts, atomic motion during mechanical response and electromigration, and synthesis of delicate metallic conformations or defect-free quantum-dot structures has just begun.

VI. Acknowledgments

The authors are grateful to the numerous researchers who have graciously supplied us with figures from their work: Dr. F. Besenbacher, Dr. H. Brune, Dr. D. D. Chambliss, Dr. T. Michely, Dr. B. Müller, Dr. A. K. Schmid, Dr. M. Schmid, Dr. E. Laegsgaard, Dr. J. A. Stroscio, and Dr. J. Tersoff. We also thank Dr. Norman C. Bartelt for his careful reading and comments of the manuscript. The preparation of this review was supported by the Office of Basic Energy Sciences Division of Material Science of the U.S. Department of Energy under contract number DE-AC04-94AL85000.

VII. References

(1) Hansma, P. K.; Tersoff, J. *J. Appl. Phys.* **1987**, *61*, R1.
(2) Kellogg, G. L. *Surf. Sci. Rep.* **1994**, *21*, 1.
(3) Merwe, J. H. v. d. *Treatise Mater. Sci.* **1974**, *T2*, 1.
(4) Stroscio, J. A.; Pierce, D. T.; Dragoset, R. A. *Phys. Rev. Lett.* **1993**, *70*, 3615.
(5) Stroscio, J. A.; Pierce, D. T. *Phys. Rev. B* **1994**, *49*, 8522.
(6) Bartelt, M. C.; Evans, J. W. *Phys. Rev. B* **1992**, *46*, 12675.
(7) Bartelt, M. C.; Evans, J. W. *Surf. Sci.* **1993**, *298*, 421.
(8) Amar, J. G.; Family, F. *Phys. Rev. B* **1994**, *50*, 8781.
(9) Amar, J. G.; Family, F. *Phys. Rev. Lett.* **1995**, *74*, 2066.
(10) Ratsch, C.; Zangwill, A.; Smilauer, P.; Vvedensky, D. D. *Phys. Rev. Lett.* **1994**, *72*, 3994.
(11) Ratsch, C.; Smilauer, P.; Zangwill, A.; Vvedensky, D. D. *Surf. Sci.* **1995**, *329*, L599.
(12) Breeman, M.; Barkema, G. T.; Langelaar, M. H.; Boerma, D. O. *Thin Solid Films* **1996**, *272*, 195.
(13) Bales, G. S.; Chrzan, D. C. *Phys. Rev. B* **1994**, *50*, 6057.
(14) Bales, G. S.; Zangwill, A. *Phys. Rev. B* **1997**, *55*, R1973.
(15) Venables, J. A. *Phil. Mag.* **1973**, *27*, 697.
(16) Bartelt, M. C.; Perkins, L. S.; Evans, J. W. *Surf. Sci.* **1995**, *344*, L1193.
(17) Evans, J. W.; Bartelt, M. C. *Surface Diffusion: Atomistic and Collective Processes*; Tringides, M. C., Scheffler, M., Eds.; Proc. of the NATO ASI; Plenum: New York, 1997.
(18) Feibelman, P. J. *Phys. Rev. B* **1995**, *52*, 12444.
(19) Zhang, C.-M.; Bartelt, M. C.; Wen, J.-M.; Jenks, C. J.; Evans, J. W.; Thiel, P. A. *Surf. Sci.* **1997**, in press .
(20) Breeman, M.; Barkema, G. T.; Boerma, D. O. *Surf. Sci.* **1995**, *323*, 71.
(21) Bartelt, M. C.; Günther, S.; Kopatzki, E.; Behm, R. J.; Evans, J. W. *Phys. Rev. B* **1996**, *53*, 4099.
(22) Brune, H.; Romainszyk, C.; Röder, H.; Kern, K. *Nature (London)* **1994**, *369*, 469.
(23) Kopatzki, E.; Günther, S.; Nichtl-Pecher, W.; Behm, R. J. *Surf. Sci.* **1993**, *284*, 154.
(24) Linderoth, T. R.; Mortensen, J. J.; Jacobsen, K. W.; Laegsgaard, E.; Stensgaard, I.; Besenbacher, F. *Phys. Rev. Lett.* **1996**, *77*, 87.
(25) Bott, M.; Hohage, M.; Morgenstern, M.; Michely, T.; Comsa, G. *Phys. Rev. Lett.* **1996**, *76*, 1304.
(26) Tsui, F.; Wellman, J.; Uher, C.; Clarke, R. *Phys. Rev. Lett.* **1996**, *76*, 3164.
(27) Brune, H.; Röder, H.; Boragno, C.; Kern, K. *Phys. Rev. B* **1994**, *49*, 2997.
(28) Müller, B.; Nedelmann, L.; Fischer, B.; Brune, H.; Kern, K. *Phys. Rev. B* **1996**, *54*, 17858.
(29) Meyer, J. A.; Behm, R. J. *Surf. Sci.* **1995**, *322*, L275.
(30) Elkinani, I.; Villain, J. *J. Phys. I Fr.* **1994**, *4*, 949.
(31) Evans, J. W.; Sanders, D. E.; Thiel, P. A.; DePristo, A. E. *Phys. Rev. B* **1990**, *41*, 5410.
(32) Evans, J. W. *Phys. Rev. B* **1991**, *43*, 3897.
(33) Bartelt, M. C.; Evans, J. W. *Phys. Rev. Lett.* **1995**, *75*, 4250.
(34) Bartelt, M. C.; Evans, J. W. *MRS Symp. Proc.* **1996**, *399*, 89.
(35) Stroscio, J. A.; Pierce, D. T.; Stiles, M.; Zangwill, A.; Sander, L. M. *Phys. Rev. Lett.* **1995**, *75*, 4246.
(36) Amar, J. G.; Family, F. *Phys. Rev. B* **1996**, *54*, 14748.
(37) Elliott, W. C.; Miceli, P. F.; Tse, T.; Stephens, P. W. *Physica B* **1996**, *221*, 65.
(38) Wulfhekel, W.; Lipkin, N. N.; Kliewer, J.; Rosenfeld, G.; Jorritsma, L. C.; Poelsema, B.; Comsa, G. *Surf. Sci.* **1996**, *348*, 227.
(39) Stoyanov, S.; Markov, I. *Surf. Sci.* **1982**, *116*, 313.
(40) Cohen, P. I.; Petrich, G. S.; Pukite, P. R.; Whaley, G. J. *Surf. Sci.* **1989**, *216*, 222.
(41) Petrich, G. S.; Pukite, P. R.; Wowchak, A. M.; Whaley, G. J.; Cohen, P. I.; Arrott, A. S. *J. Cryst. Growth* **1989**, *95*, 23.
(42) Kariotis, R.; Lagally, M. G. *Surf. Sci.* **1989**, *216*, 557.
(43) Resh, J.; Strozier, J.; Bensaoula, A.; Ignatiev, A. *J. Vac. Sci. Technol. A* **1991**, *9(3)*, 1551.
(44) Meyer, J. A.; Vrijmoeth, J.; Vegt, H. A. v. d.; Vlieg, E.; Behm, R. J. *Phys. Rev. B* **1995**, *51*, 14790.
(45) Smilauer, P.; Harris, S. *Phys. Rev. B* **1995**, *51*, 14798.
(46) Tersoff, J.; Gon, A. W. D. v. d.; Tromp, R. M. *Phys. Rev. Lett.* **1994**, *72*, 266.
(47) Bromann, K.; Brune, H.; Röder, H.; Kern, K. *Phys. Rev. Lett.* **1995**, *75*, 677.
(48) Schröder, J.; Günther, C.; Hwang, R. Q.; Behm, R. J. *Ultramicroscopy* **1992**, *42*−*44*, 475.
(49) Hwang, R. Q.; Günther, C.; Schröder, J.; Günther, S.; Kopatzki, E. *J. Vac. Sci. Technol. A* **1992**, *10*, 1970.
(50) Esch, S.; Hohage, M.; Michely, T.; Comsa, G. *Phys. Rev. Lett.* **1994**, *72*, 518.
(51) Vegt, H. A. v. d.; Pinxteren, H. M. v.; Lohmeier, M.; Vlieg, E.; Thorton, J. M. C. *Phys. Rev. Lett.* **1992**, *68*, 3335.
(52) Rosenfeld, G.; Servaty, R.; Teichert, C.; Poelsema, B.; Comsa, G. *Phys. Rev. Lett.* **1993**, *71*, 895.
(53) Vrijmoeth, J.; Vegt, H. A. v. d.; Meyer, J. A.; Vlieg, E.; Behm, R. J. *Phys. Rev. Lett.* **1994**, *72*, 3843.
(54) Oppo, S.; Fiorentini, V.; Scheffler, M. *Phys. Rev. Lett.* **1993**, *71*, 2437.
(55) Kunkel, R.; Poelsema, B.; Verheij, L. K.; Comsa, G. *Phys. Rev. Lett.* **1990**, *65*, 733.
(56) Bott, M.; Michely, T.; Comsa, G. *Surf. Sci.* **1992**, *272*, 161.
(57) Hwang, R. Q.; Schröder, J.; Günther, C.; Behm, R. J. *Phys. Rev. Lett.* **1991**, *67*, 3279.
(58) Hohage, M.; Bott, M.; Morgentstern, M.; Zhang, Z.; Michely, T.; Comsa, G. *Phys. Rev. Lett.* **1996**, *76*, 2366.
(59) Brune, H.; Röder, H.; Bromann, K.; Kern, K.; Jacobsen, J.; Stoltze, P.; Jacobsen, K.; Norskov, J. *Surf. Sci.* **1996**, *349*, L115.
(60) Merwe, J. H. v. d. *Interface Sci.* **1996**, *3(4)*, 303.
(61) Günther, C.; Vrijmoeth, J.; Hwang, R. Q.; Behm, R. J. *Phys. Rev. Lett.* **1995**, *74*, 754.
(62) Pötschke, G. O.; Behm, R. J. *Phys. Rev. B* **1991**, *44*, 1442.
(63) Hwang, R. Q.; Hamilton, J. C.; Stevens, J. L.; Foiles, S. M. *Phys. Rev. Lett.* **1995**, *75*, 4242.
(64) Hirth, J. P.; Lothe, J. *Theory of Dislocations*; John Wiley & Sons, Inc.: New York, 1992.
(65) Carter, C. B.; Hwang, R. Q. *Phys. Rev. B* **1995**, *51*, 4730.
(66) Frank, F. C.; Merwe, J. H. v. d. *Proc. R. Soc. London* **1948**, *198*, 205.
(67) Hamilton, J. C.; Foiles, S. M. *Phys. Rev. Lett.* **1995**, *75*, 882.
(68) Jacobsen, J.; Nielsen, L. P.; Besenbacher, F.; Stensgaard, I.; Laegsgaard, E.; Rasmussen, T.; Jacobsen, K. W.; Norskov, J. K. *Phys. Rev. Lett.* **1995**, *75*, 489.
(69) Nagl, C.; Schmid, M.; Varga, P. *Surf. Sci.* **1996**, *369*, 159.
(70) Foiles, S. M. *Surf. Sci.* **1993**, *292*, 5.
(71) Mottet, C.; Treglia, G.; Legrand, B. *Phys. Rev. B* **1992**, *46*, 16018.
(72) Müller, B.; Fisher, B.; Nedelmann, L.; Fricke, A; Kern, K. *Phys. Rev. Lett.* **1996**, *76*, 2358.
(73) Nedelmann, L.; Müller, B.; Fischer, B.; Kern, K.; Erdös, D.; Wollschläger, J.; Henzler, M. *J. Vac. Sci. Technol. A* **1996**, *14-(31)*, 1878.
(74) Schmid, A. K.; Bartelt, N. C.; Hamilton, J. C.; Carter, C. B.; Hwang, R. Q. *Phys. Rev. Lett.* **1997**, *78*, 3507.
(75) Chambliss, D. D.; Wilson, R. J.; Chiang, S. *Phys. Rev. Lett.* **1991**, *66*, 1721.
(76) Chambliss, D. D.; Wilson, R. J.; Chiang, S. *J. Vac. Sci. Technol. A* **1992**, *10(4)*, 1993.
(77) Speckmann, M.; Oepen, H. P.; Ibach, H. *Phys. Rev. Lett.* **1995**, *75*, 2035.
(78) Stroscio, J. A.; Pierce, D. T.; Dragoset, R. A.; First, P. N. *J. Vac. Sci. Technol. A* **1981**, *10(4)*, 1981.
(79) Chambliss, D. D.; Wilson, R. J.; Chiang, S. *IBM J. Res. Dev.* **1995**, *39*, 639.
(80) Rousset, S.; Chiang, S.; Fowler, D. E.; Chambliss, D. D. *Surf. Sci.* **1993**, *287*, 941.
(81) Chiang, S.; Rousset, S.; Fowler, D. E.; Chambliss, D. D. *J. Vac. Sci. Technol. B* **1994**, *12(3)*, 1747.
(82) Chambliss, D. D.; Chiang, S. *Surf. Sci.* **1992**, *264*, L187.

(83) Chambliss, D. D.; Johnson, K. E.; Wilson, R. J.; Chiang, S. J. *Magnetism and Magnetic Mater.* **1993**, *121*, 1.
(84) Chang, S.-L.; Wen, J.-W.; Thiel, P. A.; Günther, S.; Meyer, J. A.; Behm, R. J. *Phys. Rev. B* **1996**, *53*, 13747.
(85) Röder, H.; Shuster, R.; Brune, H.; Kern, K. *Phys. Rev. Lett.* **1993**, *71*, 2086.
(86) Murray, P. W.; Thorshaug, S.; Stensgaard, I.; Besenbacher, F.; Laegsgaard, E. *Phys. Rev. B* **1997**, *55*, 1380.
(87) Wang, Z. Q.; Li, Y. S.; Lok, C. K. C.; Quinn, J.; Jona, F.; Marcus, P. M. *Solid State Commun.* **1987**, *62*, 181.
(88) Foiles, S. M. *Surf. Sci.* **1987**, *191*, 329.
(89) Murray, P. W.; Stensgaard, I.; Laegsgaard, E.; Besenbacher, F. *Phys. Rev. B* **1995**, *52*, R14404.
(90) Flores, T.; Junghans, S.; Wuttig, M. *Surf. Sci.* **1997**, *371*, 1.
(91) Barth, J. V.; Brune, H.; Schuster, R.; Behm, R. J. *Surf. Sci.* **1993**, *292*, L769.
(92) Rousset, S.; Chiang, S.; Fowler, D. E.; Chambliss, D. D. *Phys. Rev. Lett.* **1992**, *69*, 3200.
(93) Schmid, A. K.; Atlan, D.; Itoh, H.; Heinrich, B.; Ichinokawa, T.; Kirschner, J. *Phys. Rev. B* **1993**, *48*, 2855.
(94) Figuera, J. d. l.; Prieto, J. E.; Kostka, G.; Müller, S.; Ocal, C.; Miranda, R.; Heinz, K. *Surf. Sci.* **1996**, *349*, L139.
(95) Shen, J.; Giergiel, J.; Schmid, A. K.; Kirschner, J. *Surf. Sci.* **1995**, *328*, 32.
(96) Nagl, C.; Platzgummer, E.; Schmid, M.; Varga, P. *Phys. Rev. Lett.* **1995**, *75*, 2976.
(97) Chambliss, D.; Wilson, R. J.; Chiang, S. *J. Vac. Sci. Technol. A* **1993**, *10(4)*, 1993.
(98) Johnson, K. E.; Chambliss, D. D.; Wilson, R. J.; Chiang, S. *J. Vac. Sci. Technol. A* **1993**, *11(4)*, 1654.
(99) Johnson, K. E.; Chambliss, D. D.; Wilson, R. J.; Chiang, S. *Surf. Sci.* **1994**, *313*, L811.
(100) Nielsen, L. P.; Besenbacher, F.; Stensgaard, I.; Laegsgaard, E.; Engdahl, C.; Stoltze, P.; Norskov, J. K. *Phys. Rev. Lett.* **1995**, *74*, 1159.
(101) Tersoff, J. *Phys. Rev. Lett.* **1995**, *74*, 434.
(102) Keating, P. N. *Phys. Rev.* **1966**, *145*, 637.
(103) Stevens, J. L.; Hwang, R. Q. *Phys. Rev. Lett.* **1995**, *74*, 2078.
(104) Schmid, A. K.; Hamilton, J. C.; Bartelt, N. C.; Hwang, R. Q. *Phys. Rev. Lett.* **1996**, *77*, 2977.
(105) Hwang, R. Q. *Phys. Rev. Lett.* **1996**, *76*, 4757.
(106) Swartzentruber, B. S. *Phys. Rev. Lett.* **1996**, *76*, 459.

CR960070H